

Integrated field, satellite and petrological observations of the November 2010 eruption of Erta Ale

Lorraine Field · Talfan Barnie · Jon Blundy ·
Richard A. Brooker · Derek Keir · Elias Lewi ·
Kate Saunders

Received: 5 January 2012 / Accepted: 10 September 2012 / Published online: 12 October 2012
© Springer-Verlag Berlin Heidelberg 2012

Abstract Erta Ale volcano, Ethiopia, erupted in November 2010, emplacing new lava flows on the main crater floor, the first such eruption from the southern pit into the main crater since 1973, and the first eruption at this remote volcano in the modern satellite age. For many decades, Erta Ale has contained a persistently active lava lake which is ordinarily confined, several tens of metres below the level of the main crater, within the southern pit. We combine on-the-ground field observations with multispectral imaging from the SEV-IRI satellite to reconstruct the entire eruptive episode beginning on 11 November and ending prior to 14 December 2010. A period of quiescence occurred between 14 and 19 November. The main eruptive activity developed between 19 and 22 November, finally subsiding to pre-eruptive levels

between 8 and 15 December. The estimated total volume of lava erupted is $\sim 0.006 \text{ km}^3$. The mineralogy of the 2010 lava is plagioclase+clinopyroxene+olivine. Geochemically, the lava is slightly more mafic than previously erupted lava lining the caldera floor, but lies within the range of historical lavas from Erta Ale. SIMS analysis of olivine-hosted melt inclusions shows the Erta Ale lavas to be relatively volatile-poor, with H_2O contents $\leq 1,300$ ppm and CO_2 contents of ≤ 200 ppm. Incompatible trace and volatile element systematics of melt inclusions show, however, that the November 2010 lavas were volatile-saturated, and that degassing and crystallisation occurred concomitantly. Volatile saturation pressures are in the range 7–42 MPa, indicating shallow crystallisation. Calculated pre-eruption and melt inclusion entrapment temperatures from mineral/liquid thermometers are $\sim 1,150$ °C, consistent with previously published field measurements.

Editorial responsibility: J.E. Gardner

Electronic supplementary material The online version of this article (doi:10.1007/s00445-012-0660-7) contains supplementary material, which is available to authorized users.

L. Field (✉) · J. Blundy · R. A. Brooker · K. Saunders
School of Earth Sciences, University of Bristol,
Queen's Road,
Bristol BS8 1RJ, UK
e-mail: l.p.field@gmail.com

T. Barnie
Department of Geography, University of Cambridge,
Downing Place,
Cambridge CB2 3EN, UK

D. Keir
National Oceanography Centre Southampton,
University of Southampton Waterfront Campus,
European Way,
Southampton SO14 3ZH, UK

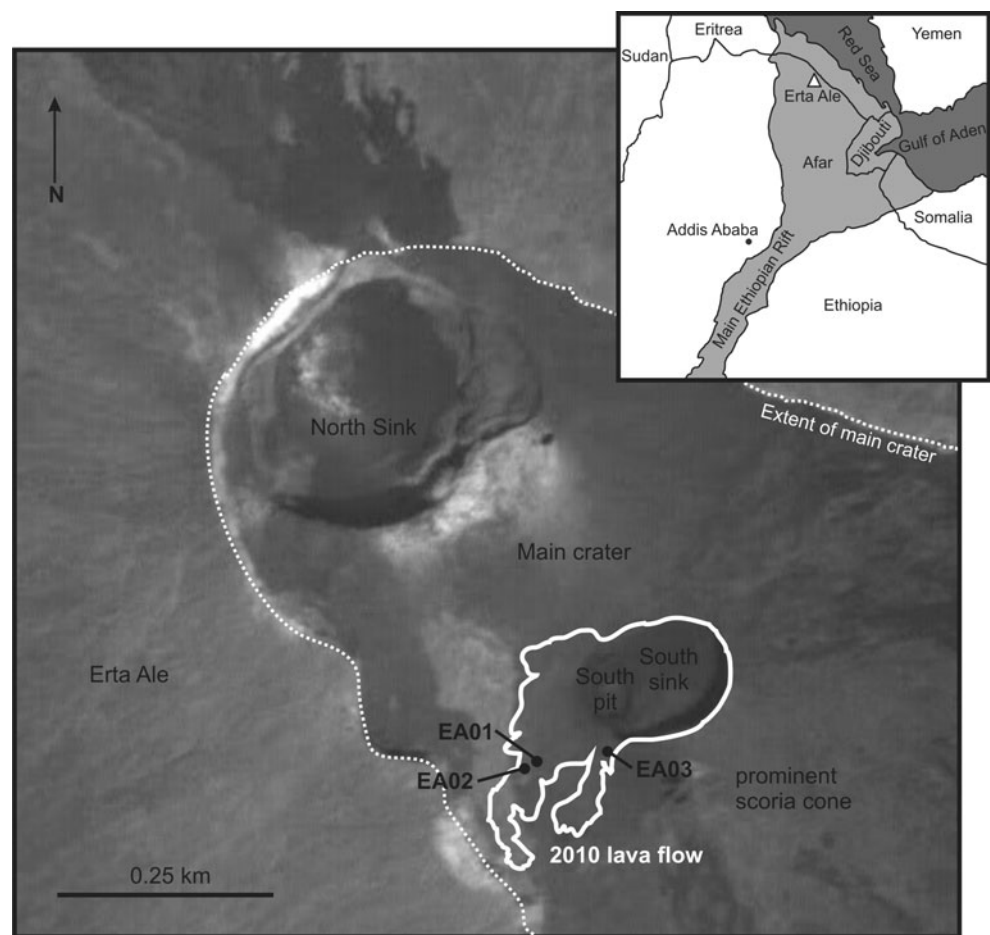
E. Lewi
Geophysical Observatory, University of Addis Ababa,
Addis Ababa, Ethiopia

Keywords Afar · Ethiopia · Remote sensing of volcanoes · Lava lake · Melt inclusions · Basalt

Introduction

The Afar depression lies at the triple junction between the Red Sea, Gulf of Aden and East African rifts, and has been produced by rifting between Africa and Arabia over the past ~ 30 Myr (Wolfenden et al. 2005). The southern Red Sea rift has become punctuated over the past ~ 3 million years with ~ 60 -km long magmatic segments as faulting and volcanic activity have become more focused into localised regions (Barberi and Varet 1977). Erta Ale is a basaltic shield volcano ($13^\circ 36' 11.41''\text{N}$, $40^\circ 39' 50.08''\text{E}$) situated within the Erta Ale magmatic segment (Fig. 1) which comprises six main volcanic centres (Barberi and Varet 1970). The Erta Ale segment is the northernmost in Afar and forms the sub-aerial southwards

Fig. 1 Sketch map indicating the location of Erta Ale and satellite image of the Erta Ale crater, with the extent of the November–December 2010 eruption lavas [$\sim 0.4 \text{ km}^2$: GPS track courtesy of James Hammond (February 2011)]. Sample locations from 22 November are shown, which were subsequently covered by further overflows. Image taken by the PRISM instrument on ALOS satellite, with an image resolution of 2.5 m. Image acquired on 19 November 2008. Data acquired from ESA



continuation of the Red Sea rift (Prodehl et al. 1997). The last eruption in this segment occurred in November 2008 when basaltic lava covered 15 km^2 , originating from a fissure between Dalaffilla and Alu volcanoes (Pagli et al. 2012).

Erta Ale is known for its active lava lakes situated in the northern and southern pits within a main 0.7×1.6 -km elliptical summit crater (Fig. 1; a summary of recorded activity is provided in Supplementary Table 5). The Erta Ale lava lake is one of just four long-lived lava lakes existing across the world; others are Erebus (Antarctica), Nyiragongo (DR Congo) and Ambrym (Vanuatu). Shorter-lived lava lakes also appear elsewhere periodically, e.g. Kilauea, Hawaii and Villarrica, Chile.

The first systematic study of the Erta Ale lava lake began in 1967 (Barberi and Varet 1970), but the lake is likely to have existed from much earlier than this, as reports of a ‘smoking mountain’ and characteristic red summit glow were recorded by early visitors to the area (e.g. Nesbitt 1935; Dainelli and Marinelli 1907; Barberi and Varet 1970). Erta Ale volcano is remote and difficult to access, and as a result, observations have been sporadic: it was not until the CNR-CNRS campaigns of the late 1960s that it began to be studied in detail (e.g. Barberi and Varet 1970; Tazieff 1973). At this time, a lava lake existed in both the northern and southern pits, but the

northern lake solidified between 1988 and 1992 following emplacement of two lava flows during this period (Vetsch et al. 1992). The southern lake’s surface solidified briefly between late 2004 and April 2005 (Bardintzeff and Gaudru 2004; Yirgu and Philpotts 2005). It was reactivated in September 2005, with lava visibly overturning at the edges of the lava lake, within the pit, possibly in response to the volcano-seismic crisis in Afar (Ayele et al. 2007). The level of the southern lake has fluctuated (Le Guern et al. 1979), but the majority of recent observations indicate the lake level was generally tens of metres below the floor of the main crater, nestled at the base of the southern pit (e.g. Oppenheimer and Francis 1997). Eruptions occur from these lakes from time to time, causing lava to overflow from the pits onto the main crater floor, but they are rarely observed. Varet (1972a), reported the first recorded eruptive event from the southern pit in March 1972, following the emplacement of two new lava flows into the main crater which emanated from the southern side of the south pit; one sometime prior to 21 and one on 23 of March. This activity continued with three additional new lava flows, visible when the volcano was visited in May 1972 (Varet 1972b). Tazieff (1973) reported overflows which overran the main crater rim in March 1973. From this occurrence until November 2010, no further

recorded observations were made of the southern pit filling and overflowing into the main crater in an eruptive event, or of the appearance of any fresh lava flows.

Ground observations

Ground observations began on 21 November 2010 at ~1600 hours UTC (Co-ordinated Universal Time). The team were unaware on approaching the volcano of any eruptive activity, and no visible signs, e.g. plume, could be seen on the 8-km hike up to the crater; however, on arrival, the eruption was underway (Table 1). Observations from the previous few years located the lava lake at the base of the pit, ~20 m depth. However, the pit had filled with lava, level with the main crater floor on the western side (Figs. 1 and 2). The first overflow of lava onto the main crater floor occurred at ~1650 hours UTC (Fig. 3a). An embryonic scoria ring cone had built up around the lake, similar to that observed in 1973 (Tazieff 1973). Overflows out of the scoria cone into the pit, and occasionally on to the main crater floor, continued at approximately 2-h intervals until ~1430 hours UTC on 22 November. Video footage indicates the lava was of low

viscosity (Supplemental Video 1). Lava flows were inflated by volatiles and thus had hollow interiors. For the remainder of the ground observation, the lake was contained within the scoria ring cone, which by 0300 hours UTC on 23 November had grown to ~4 m high on the southern side. The lava lake level rose and fell by ~4 m on a ~20-min cycle, with agitated Strombolian activity at the peak of each cycle. Between the peaks, activity at the lake surface was more subdued and constrained within the scoria ring with sporadic bubble-bursting, rather than larger-scale fire-fountaining. On the morning of 23 November, the northern side of the scoria ring cone suffered partial collapse. Blue-green gas jets could be seen periodically at various points across the lava lake, some remaining stable for several hours. New lava flows were visible within the northern pit, together with some incandescence during the night of 21 November. After departing from the summit on 23 November, a small but distinct plume was visible above the volcano from the surrounding plain.

Satellite imaging

Method

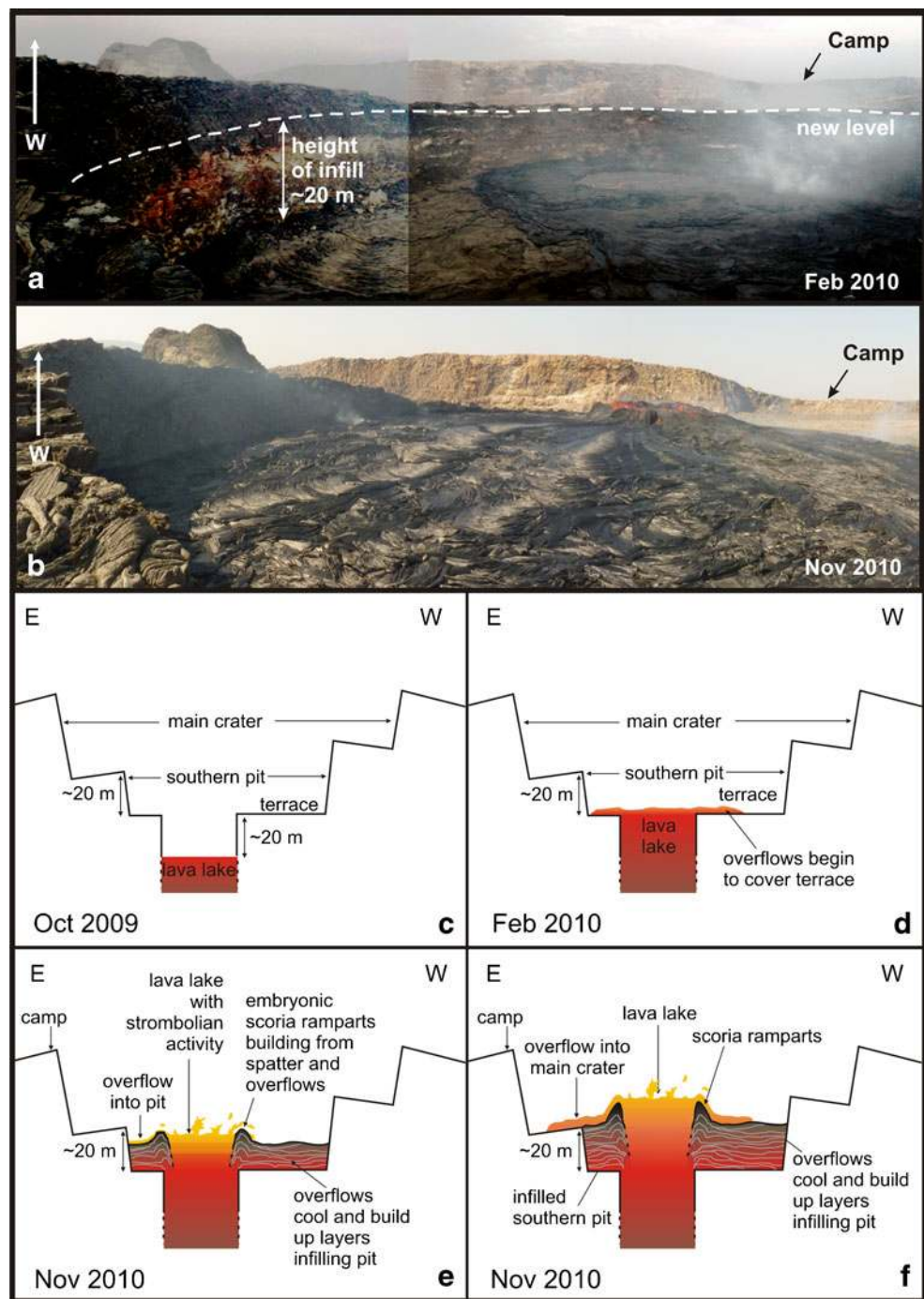
The SEVIRI instrument is a multispectral imager aboard the second generation of Meteosat geostationary weather satellites. The Meteosat 9 satellite is positioned over 0°E, 0°N, and the on-board SEVIRI instrument images the full Earth disc visible from this position every 15 min in 12 bands. Four of these bands are useful for monitoring thermal radiation from volcanic products, at wavelengths of 1.6, 3.9, 10.8 and 12.0 μm (e.g. Hirn et al. 2009). The resolution of the image at the sub-satellite point is 3 km, but this increases towards the edge of the image due to the constant angular sampling of the instrument and the curvature of the Earth, so that at Erta Ale, the resolution is approximately 4 km in the E–W direction and 5 km in the N–S direction (Müller 2010). Due to the stable viewing geometry of the instrument, each pixel images the same area of the Earth's surface at the same view angle in successive images, so a sequence of radiance measurements from a given pixel is directly comparable. This is in contrast with instruments on low Earth orbit satellites such as AVHRR and MODIS, where for a given volcanic feature, the observing pixel location, size and view geometry vary substantially with each acquisition, making inter-image comparisons difficult.

We acquired 9,802 Meteosat 9 SEVIRI images of the Erta Ale region between 1 October 2010 and 10 January 2011. The images were converted to radiance using the gain and offset values stored in the image headers, and the time series of radiance values for the pixel covering the Erta Ale lava lake was extracted, giving a 15-min time resolution record

Table 1 Summary timetable of ground observations

| Date | Approximate times (UTC) | Comment |
|---------------|-------------------------|----------------------------------------------------------------------------------------------------------------------------------------------------------------------------|
| 21st November | 1300 | Base of volcano, no visible signs of eruption, e.g. plume |
| | 1600 | Arrival of field team at volcano Southern pit infilled with lava; lava lake was agitated with frequent fire fountaining. Embryonic scoria ring had built up around lake |
| | 1650 | First overflow of lava onto main crater floor |
| | 1850 onwards | Overflows of lava from the lake, onto pit floor and occasionally onto main crater floor occurred at approximately 2-h intervals |
| 22nd November | 1430 | Overflows ceased Lava lake rose and fell by ~4 m on a ~20-min cycle with agitated Strombolian activity at height of cycle |
| 23rd November | Overnight | Incandescent gas jets visible, some burning for several hours |
| | 0400 | Scoria ring now ~4 m high on southern side; northern side suffered partial collapse |
| | 0500 | Field team left summit of Erta Ale |
| | 0700 | Field team at base of volcano; distinct plume visible |

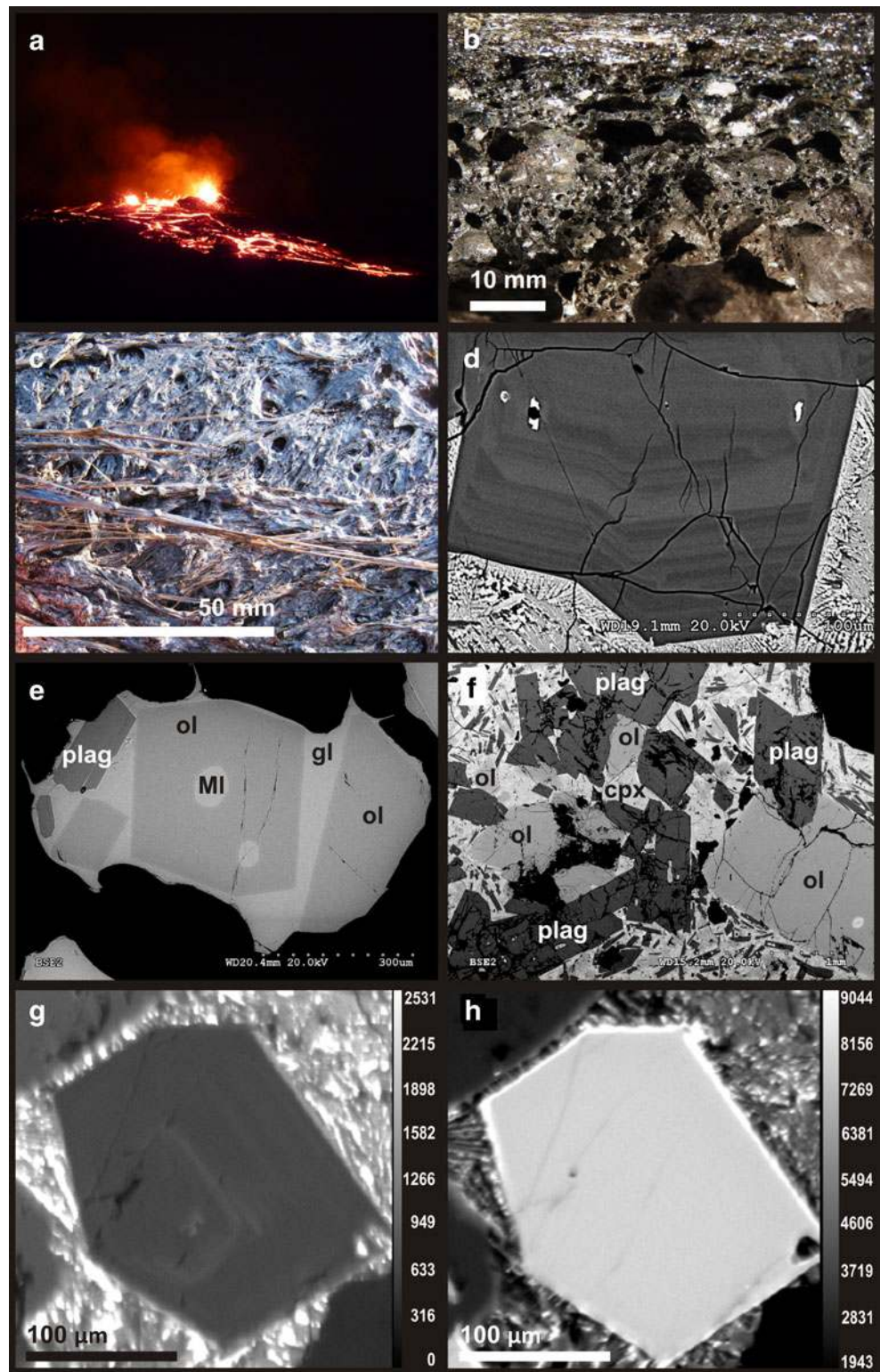
Fig. 2 Comparison of the lava levels in the south sink between (a) February 2010 and (b) 22 November 2010. The lava has filled a depth of ~20 m. The February 2010 level is similar to that observed on the 11 and 14 November (J. Wilkinson, personal communication). c–f Cartoon cross-sections of the Erta Ale lava lake from observations by members of the field team: (c) October 2009, (d) February 2010 and (e, f) stages in the eruption of November 2010 indicating the formation of the scoria ramparts and infilling of the southern pit and sink



of the radiant output of the eruption. Thermal anomalies were only observed in the 3.9- μm band, consistent with the presence of a very small surface area at volcanic temperatures. Larger areas would register at the 10.8- and 12.0- μm bands, saturate the 3.9- μm band and, if there was enough incandescent material (e.g. cracks, fire fountains and shear zones), also register at the 1.6- μm band (Davies et al. 2010). We subtracted the radiance from a neighbouring cold pixel to obtain the excess radiance emitted by the hot volcanic material, over and above that radiated and reflected by a

region with similar reflective and emissive properties at background temperatures. This gives us a time series of the thermal anomaly associated with the eruption, which we interpret qualitatively. The lava lake and background pixel do have subtle differences in radiance patterns in the absence of hot material in the lava lake pixel, and as a result, there is a regular small dip in the thermal anomaly at dawn; however, this effect is small and does not invalidate our observations, which are first order and qualitative in nature.

Fig. 3 **a** Emplacement of first observed overflow (sample EA001) ~1650 hours UTC on 21 November 2010. **b** Close-up of a section through the fresh lava showing the glassy surface, plagioclase-rich layer and vesicular core. **c** Close-up of the surface of the new lava. **d** BSE image of oscillatory-zoned plagioclase rim from sample EA001 with quenched glass matrix. **e** Euhedral olivine and melt inclusion from sample EA003. **f** Sample EA002, the underlying lava flow, which has a fine-grained groundmass. In **g** and **h** $K\alpha$ X-ray intensity maps in an olivine from sample EA001 are shown. **g** Combined phosphorous image from four spectrometers shows faint zoning throughout the crystal. **h** Example major element (Fe) map shows no visible zoning



Interpretation

The Erta Ale lava lake does not typically register in any SEVIRI band, despite being frequently observed by MODIS (e.g. Ayele et al. 2007; Wright and Pilger 2008). This is a

function of look angle; the MODIS instruments view the lava lake from a range of angles, while SEVIRI views from a constant angle of $\sim 42^\circ\text{E}$, at which the lake is completely occluded from the sensor field of view by the crater rim when the lava lake is at a low stand

(typically ~20 m below the surface). As the lava lake level rises, or overflows onto the pit floor, more of the surface area of the lava comes into view of the sensor. This increases the measured radiance, resulting in a

thermal anomaly when compared with neighbouring pixels containing no hot lava. The thermal anomaly varies over two time periods, one on a timescale of days, the other on a timescale of hours (Fig. 4).

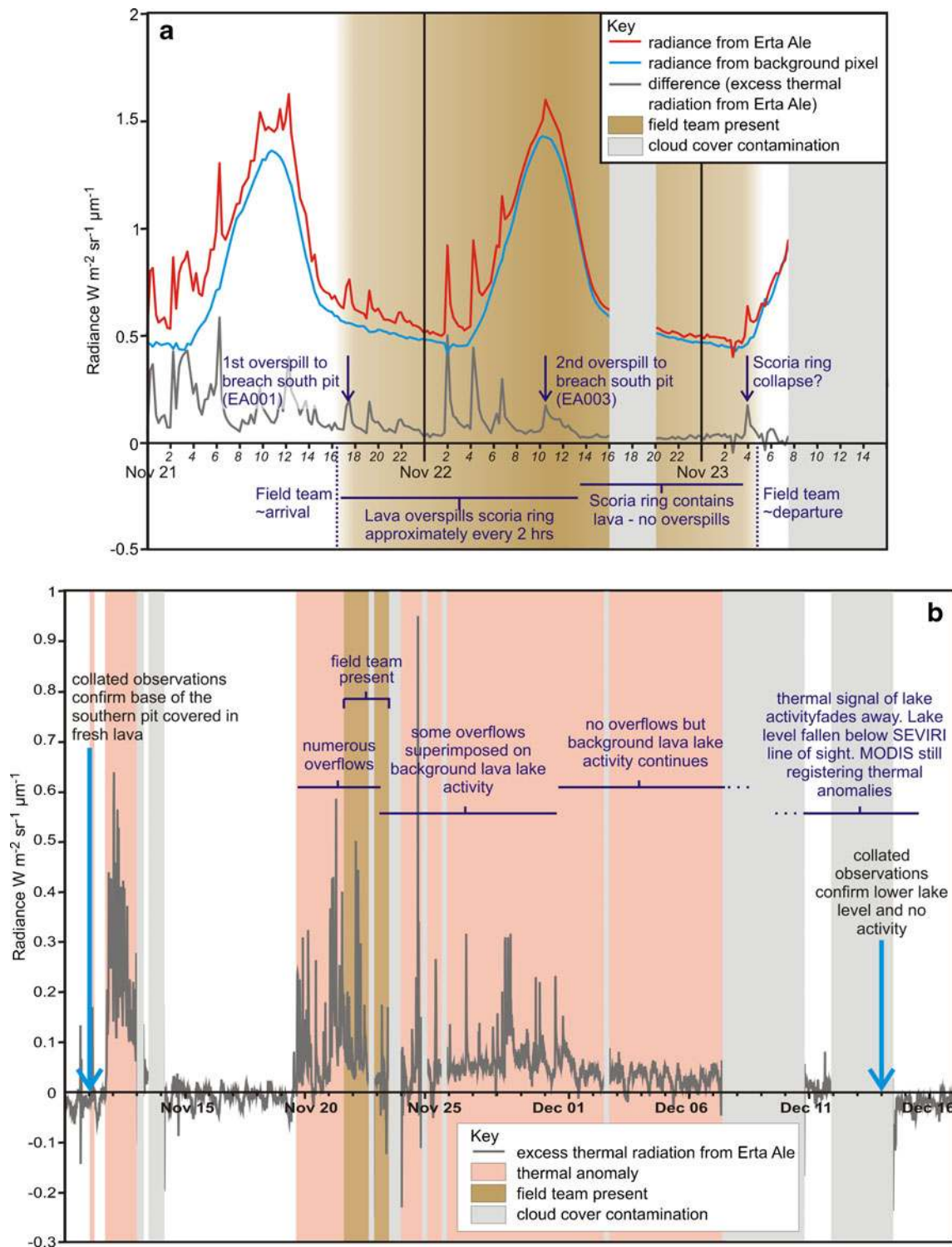


Fig. 4 SEVERI thermal signal of Erta Ale compared to contemporaneous ground observations. **a** Detail from when field team were present at Erta Ale showing the radiance from lava and background, and the

difference, i.e. the excess thermal radiation. Time in UTC. **b** Overall image of the eruption showing the excess thermal radiation graph only

The variation on a timescale of hours is characterised by sharp increases in radiance over a period of <15 min, followed by an exponential decay over a period of around an hour. These spikes in radiance have been correlated with lava overflows observed in the field, so we interpret the spikes as lava overflows: either initially onto the ‘terrace’ abutting the lake within the pit as the lake level rises or over the scoria ramparts surrounding the high stand lake, onto the new infilled surface of the pit and eventually onto the main crater floor. The rapid rise in radiance over 15 to 30 min associated with each spike is interpreted as the advance of the overflow; the subsequent exponential decay in radiance over a period of a few hours is the cooling of the surface. Each overflow can be considered a temporary increase in the area of the ‘lava lake’. Between spikes, the background radiance from the lava lake varies little as the lava lake level remains relatively constant, which we interpret to mean the surface temperature distribution varies little.

The second thermal anomaly variance is on a timescale of days. A thermal anomaly is present during two periods (Fig. 4b). The first starts with an isolated spike in radiance at 0212 hours UTC on 11 November, which decays to the background level after about an hour. The anomaly reappears slightly later at 1557 hours UTC, peaks around midnight on 11 November and then decays to 0657 hours UTC on 13 November. This overall trend is punctuated by numerous spikes in radiance. The second period begins on 1442 hours UTC on 19 November and is marked by numerous spikes in radiance. It continues until ~1457 hours UTC on 22 November. The baseline anomaly then slowly increased with markedly fewer radiance spikes to approximately midnight on 30 November. After this time, the background radiance drops to a lower level and remains at approximately this level until early morning on 7 December, when the lava lake became obscured by cloud. The thermal anomaly decays to background between 8 December and 15 December.

This pattern in the long timescale variation in the thermal anomaly could be due to changes in lava lake height (and therefore occlusion by the rim), changes in lava lake area, surface temperature distribution, Strombolian activity, overflows or renewal of activity in the solidified northern lake. Comparison with ground observations allows us to discriminate between these possibilities. From field observations, we know the period over which the lake level rose from the former position of ~20 m below the rim to the surface, and this corresponds with a period of steadily increasing background radiance. The final area of the lava lake at high stand is also similar to the initial area (~500 m²). We therefore infer that the long timescale variation in radiance is primarily a function of varying degrees of occlusion of a lava lake of a roughly constant area as a result of changes in lake height, rather than a variation in total lake area as a result of increasing width with height within the pit, or freezing of the margins of the lake.

Radiance spikes during the period of ground observations correlate with overflows and collapses, while a steady low-level radiance anomaly between spikes correlates with background lake activity. The sampling interval of 15 min is insufficient to resolve the observed 20-min variation in lake height. We therefore interpret the radiance spikes as overflows, as the lava lake progressively builds itself up by first episodically flooding the pit, and then constructing the scoria ramparts by successive overflows and spatter (see Fig. 2e, f).

Petrology

Method

Three samples were collected for analysis: EA001 collected from the margin of the first overflow onto the main crater floor (Figs. 1 and 3a) and sampled approximately 12 h after emplacement; EA002 collected from the main crater floor (most likely erupted in 1973), i.e. the flow underlying the newly erupted flows; and EA003 from the last overflow observed by the field team, collected <1 h after emplacement. Whole rock major and trace elements were analysed by X-ray fluorescence (XRF) using fused glass discs and pressed powder pellets, on a PANalytical Axios-Advanced XRF spectrometer at Leicester University.

Polished thin sections were carbon-coated and imaged on a Hitachi S-3500N scanning electron microscope (SEM) prior to major element analysis using a CAMECA SX-100 electron microprobe (EMP) instrument at the University of Bristol. A 15-kV accelerating voltage, 4-nA beam current and defocused 10- μ m beam were used for matrix glasses and feldspars, and 20-kV accelerating voltage, 10-nA beam current and a focused beam (1 μ m) for olivines and cpx (clinopyroxene). A minimum of six analyses per phase were measured in each thin section.

Olivine crystals were handpicked from a crushed sample of EA003. The samples lose their glassy appearance towards the centre of the flow, and the matrix becomes dull more than ~2-cm depth from the surface. Phenocrysts picked for analysis were taken from the rapidly cooled, glassy upper 2 cm of the samples, mounted in resin and cold-cured for 2 weeks prior to polishing. Petrographic observation ensured all mounted grains contained melt inclusions (Fig. 3e). These were examined and mapped on the SEM uncoated, under variable vacuum, to minimise carbon contamination. Any melt inclusions that showed obvious signs of post-entrapment crystallisation, fractures or re-entrants were rejected. All melt inclusions were bubble-free. Eleven spot analyses from five separate melt inclusions were made, analysing for CO₂, H₂O and a number of trace elements by secondary ion mass spectrometry (SIMS) using a Cameca ims4f instrument at the

University of Edinburgh Ion Microprobe Facility. Two analyses of matrix glass were made for CO₂ and H₂O. We used a 10-kV (nominal) O⁻ primary beam and 4,500 eV positive secondary ions with offset applied to reduce transmission of molecular ions. To enhance relief, grain mounts were polished with 0.3- μ m alumina for 30 s prior to gold coating. CO₂ (¹²C⁺) was determined first at sufficient mass resolution (\sim 1,600) to separate ²⁴Mg²⁺ from ¹²C⁺ because both ions have the same mass-to-charge ratio. A 5-nA primary beam, with a 15- μ m focused spot was used, with 50 eV offset. Twenty-five- and two hundred fifty-micrometre lenses were activated to give a 60- μ m image field with field aperture No. 2 providing a \sim 15–20- μ m restricted central area for analysis. Entrance slits were set at \sim 110 (entrance) and 112 (exit). A 2-min pre-sputter with a 15- μ m raster removed surface contamination prior to using a static spot for analysis. For subsequent H₂O and trace element determinations, a 5-nA primary beam with 75 eV offset and 30 s pre-sputter was focused in the same location as the CO₂ analysis. Secondary ions of ¹H⁺, ⁹Be⁺, ¹¹B⁺, ¹²C²⁺, ²⁴Mg²⁺, ²⁶Mg⁺, ³⁰Si⁺, ⁴²Ca⁺, ⁴⁴Ca⁺, ⁴⁵Sc⁺, ⁴⁷Ti⁺, ⁸⁸Sr⁺, ⁸⁹Y⁺, ⁹⁰Zr⁺, ⁹³Nb⁺, ¹³⁸Ba⁺, ¹³⁹La⁺, ¹⁴⁰Ce⁺, ¹⁴¹Pr⁺, ¹⁴³Nd⁺, ¹⁴⁹Sm⁺, ¹⁵⁹Tb⁺, ¹⁶¹Dy⁺, ¹⁶⁵Ho⁺, ¹⁶⁶Er⁺, ¹⁷¹Yb⁺, ¹⁷⁸Hf⁺, ¹⁸¹Ta⁺, ²³²Th⁺ and ²³⁸U⁺ were collected at low mass resolution, with a 25- μ m image field and field aperture No. 2 providing \sim 10 μ m area of analysis. Calibration and secondary standards included a range of glasses of known trace element, H₂O and CO₂ values (basaltic glasses of Shishkina et al. (2010), BCR2g, TPA, TPF, SRM610 and CFD), together with an olivine crystal from Erta Ale as a monitor of background consistency.

Mid-IR spectra for H₂O and CO₂ were obtained at Bristol using a Nicolet Nexus 670 FTIR spectrometer with an IR PLAN microscope attachment, Globar source, KBr beamsplitter and MCT detector (512 scans at 8-cm⁻¹ resolution). Double-polished plates of around 50- μ m thickness were prepared and measured with Mitutoyo Digital Micrometer to \pm 1 μ m. This thickness allowed an 80- μ m beam to pass through the melt inclusions (or the matrix glass) uninterrupted. Spectra were compared to a volatile-free basalt to estimate peak heights, and these were converted to concentrations using extinction coefficients of 63 Lmol⁻¹cm⁻¹ for water at 3,550 cm⁻¹ and 375 Lmol⁻¹cm⁻¹ for one of the carbonate doublet peaks at 1,375 cm⁻¹ (from Dixon et al. (1988) and Fine and Stolper (1986), respectively). The errors in the measured IR peak intensities (due to background subtraction), the extinction coefficient, the thickness measurement and the density estimate lead to an uncertainty of about \pm 20 % for water and \pm 35 % for CO₂ in the inclusions. For the matrix glass, the CO₂ peak is not visible, suggesting it is below the detection limit of \sim 50 ppm for this sample thickness.

Major elements were determined quantitatively by EMPA on the same melt inclusions previously analysed by SIMS and on phenocryst minerals. High precision S and Cl concentration were also determined for matrix glass, one melt inclusion (J), and two small, previously unanalysed melt inclusions using two spectrometers for each element to increase total counts. The peak count was 120 s on each spectrometer. The spectrometers were calibrated using BCR2 [Basaltic glass, Columbia River (Wilson 1997)]. Oxygen was calculated by stoichiometry, and weight percent oxide totals for SO₂ are reported. K α X-ray intensity maps for phosphorous, Ca and Fe in olivine phenocrysts in EA001 were obtained in two stages. The first mapped P and Fe with a 256 \times 256 pixel image and dwell time of 100 ms per pixel. A second run at higher resolution used dwell times of 200 ms per pixel and a 512 \times 512 pixel image, imaging P and Ca. For both runs, a beam current of 400 nA, an accelerating voltage of 20 kV and beam diameter of 1 μ m was used. Phosphorous was mapped on four of the five spectrometers in both cases, and the final images were summed.

Results

The lavas are porphyritic (\sim 20 % by volume) and vesicle-rich (up to 60 % volume in EA003, calculated by point counting; see Fig. 3b), and can be classified chemically as transitional basalts (Irvine and Baragar 1971). There are surprisingly few published chemical analyses of basalts from Erta Ale volcano. To our knowledge, the only published values come from Barberi et al. (1974) and Bizouard et al. (1980) who present only major elements on two samples from Erta Ale volcano (one from the summit crater wall, and one from a western flank fissure) and Barrat et al. (1998) who present major and trace elements of four samples from the volcano. The 2010 lavas (EA001 and EA003) are olivine-normative, whereas the older underlying lava (EA002: most likely from the 1973 eruption) is quartz-normative (Table 2). The sample taken from the underlying lava has a higher silica content than the 2010 samples, comparable to the Erta Ale sample (F12) analysed by Barberi et al. (1974) from the main crater wall. This suggests the recent input to the system of less evolved but chemically similar magma. EA002 also shows significant differences in texture (Fig. 3f); a crystalline groundmass with large glomerocrysts of plagioclase, cpx and olivine, compared to the quenched glass matrix and discrete euhedral crystals found in EA001 and 3 (Fig. 3d, e). The silica contents of the 2010 samples are comparable ($<$ 50 wt.%) to those of samples analysed by Barrat et al. (1998), although the exact locality of those samples has not been ascertained. The mineral assemblage in the 2010 samples is plagioclase+clinopyroxene+olivine. No oxides or other accessory phases are present in any sample. Euhedral plagioclase phenocrysts, up to 4 mm, show

Table 2 Whole rock XRF analyses

| Sample | EA001 | EA002 | EA003 |
|---------------------------------------------|-------|--------|--------|
| <i>n</i> | 1 | 1 | 1 |
| SiO ₂ ^a (wt.%) | 48.85 | 51.36 | 49.12 |
| TiO ₂ | 1.96 | 2.13 | 1.95 |
| Al ₂ O ₃ | 16.57 | 14.88 | 16.56 |
| Fe ₂ O ₃ ^T | 10.77 | 11.38 | 10.77 |
| MnO | 0.17 | 0.17 | 0.17 |
| MgO | 6.04 | 5.61 | 6.13 |
| CaO | 12.41 | 10.86 | 12.40 |
| Na ₂ O | 2.66 | 2.62 | 2.65 |
| K ₂ O | 0.50 | 0.70 | 0.49 |
| P ₂ O ₅ | 0.27 | 0.30 | 0.27 |
| SO ₃ | b.d. | 0.42 | b.d. |
| LOI | −0.37 | 0.34 | −0.39 |
| Total | 99.81 | 100.77 | 100.10 |
| Rb | 11 | 18 | 12 |
| Sr | 310 | 318 | 315 |
| Y | 28 | 30 | 29 |
| Zr | 159 | 198 | 163 |
| Pb | 2 | 4 | 2 |
| Th | 3 | 3 | 2 |
| U | 2 | 1 | 2 |
| Ga | 19 | 19 | 19 |
| Zn | 76 | 78 | 77 |
| Cu | 106 | 96 | 109 |
| Ni | 47 | 41 | 52 |
| Co | 41 | 36 | 42 |
| Cr | 128 | 142 | 127 |
| V | 287 | 288 | 292 |
| Sc | 37 | 34 | 38 |
| Ba | 118 | 190 | 119 |
| La | 18 | 21 | 20 |
| Ce | 51 | 48 | 46 |
| Nd | 26 | 24 | 26 |
| Cs | b.d. | b.d. | b.d. |

n denotes number of analyses, *superscript* “*T*” denotes total iron

b.d. below detection level

^aMajor element analysis—XRF, University of Leicester

normal zoning from core to rim, but within some rims, oscillatory zoning is present (Fig. 3d), and there is evidence of resorption between some of the zones. Plagioclase is the dominant phenocryst comprising ~90 % of all phenocrysts. It is also found as small inclusions in both clinopyroxene and olivine, with anorthite (An) content in the range An_{83–74}. Anorthite content in plagioclase cores from the 2010 lavas (Table 3) is An_{85–69}; the range within an individual core is more restricted, e.g. An_{85–82}, An_{71–69}. Within the zoned rims, An values show a wide range from An_{80–66}, with the higher

An values found in those phenocrysts with higher An cores. A very similar range of An contents is found in EA002 (An_{82–75} in cores, An_{76–66} in rims). Plagioclase groundmass microlites are only present in EA002 and range from An_{71–63}. Clinopyroxene crystals are subhedral, small (<1 mm) augites, often forming glomerocrysts with plagioclase (Table 3). Mg# (100 × molar Mg/[Mg+Fe_{tot}]) values range from 84 to 72. One tiny (~50 μm) euhedral clinopyroxene inclusion (Mg# 82) was found in an olivine. Olivines are euhedral with Fo_{84–78} content in phenocrysts and Fo_{80–73} in rims and EA002 groundmass (Table 3).

The raw analyses of the melt inclusions indicate compositions that are close to those of the matrix glass, suggesting limited post-entrapment modification (Table 4). Using an olivine-melt K_d_{Fe-Mg} of 0.28, we estimate that post-entrapment crystallisation is less than 6 %, which would have negligible effect on the measured volatile or trace element contents. It is much more difficult to make a correction for open-system processes such as Fe diffusion through the host olivine. Consequently, the MI data have not been corrected for post-entrapment processes, and all data are reported as analysed. The H₂O content of the five inclusions ranges from 867 to 1,329 ppm; CO₂ contents range from 33 to 194 ppm (Table 4). Multiple analyses of single melt inclusions show them to be homogeneous for H₂O and CO₂. Matrix glass contains ~560 ppm H₂O and <50 ppm CO₂. FTIR values for CO₂ agree with those determined by SIMS (<50 ppm in matrix glass and 94–136 ppm in melt inclusions). FTIR H₂O values are systematically higher than SIMS, with melt inclusion values of 1,700–2,000 and 1,700 ppm in matrix glass. The source of this systematic offset is unknown, but may originate in uncertainty in the FTIR extinction coefficients or ion-yield difference for ¹H between Erta Ale glasses and the standards used. SO₂ contents of melt inclusions, measured by EMP (Table 4), are 247–419 ppm; chlorine contents are 158–368 ppm. Average SO₂ and Cl values from 25 analyses in matrix glass were determined as 91 and 195 ppm, respectively.

Temperatures were calculated using various mineral/liquid thermometers with an average of ~1,150 °C from all methods (Table 5). Pre-eruptive temperatures derived from crystal rim/matrix combinations in plagioclase/liquid (Eq. 24a, Putirka 2008) are in the range 1,171–1,180 °C, clinopyroxene/liquid (Putirka et al. 1996) temperatures are 1,148–1,175 °C, and olivine/liquid temperatures are 1,151–1,158 °C (Putirka 2008) and 1,157 °C (Beattie 1993). Temperatures derived from melt inclusion/host crystal combinations using the method of Putirka (2008) are in the range 1,094–1,148 °C, with similar temperatures (1,104–1,148 °C) obtained from the method of Beattie (1993).

Volatile saturation pressures were calculated using the method of VolatileCalc (Newman and Lowenstern 2002) and range from 7 to 40 MPa. To convert these pressures to

Table 3 Representative phenocryst analyses

| | Sample | EA001 | EA001 | EA002 | EA002 | EA003 | EA003 |
|--------------------------------|--------------------------------|-------------------------|--------|--------|--------|--------|-------|
| Plagioclase | Identifier ^a | c | r | g | c | c | r |
| | SiO ₂ ^b | 47.10 | 47.73 | 51.30 | 48.62 | 47.41 | 47.89 |
| | Al ₂ O ₃ | 32.96 | 31.48 | 29.76 | 31.11 | 31.80 | 31.44 |
| | FeO ^{Tc} | 0.57 | 0.57 | 0.72 | 0.54 | 0.50 | 0.59 |
| | MgO | 0.15 | 0.21 | 0.17 | 0.22 | 0.16 | 0.18 |
| | CaO | 16.60 | 15.53 | 13.34 | 15.24 | 15.77 | 15.64 |
| | Na ₂ O | 1.90 | 2.54 | 3.59 | 2.67 | 2.28 | 2.35 |
| | K ₂ O | b.d. | 0.11 | 0.17 | b.d. | 0.10 | 0.09 |
| | Total | 99.27 | 98.16 | 99.05 | 98.39 | 98.03 | 98.17 |
| | An | 82.84 | 76.64 | 66.54 | 75.96 | 78.81 | 78.20 |
| | Ab | 17.16 | 22.73 | 32.43 | 24.04 | 20.62 | 21.26 |
| | Or | 0.00 | 0.63 | 1.03 | 0.00 | 0.57 | 0.54 |
| | Clinopyroxene | Identifier ^a | c | r | c | g | c |
| SiO ₂ ^b | | 52.01 | 51.59 | 51.25 | 50.29 | 53.26 | 51.30 |
| TiO ₂ | | 0.76 | 0.89 | 0.93 | 1.36 | 0.64 | 0.91 |
| Al ₂ O ₃ | | 2.62 | 2.91 | 2.99 | 3.69 | 1.85 | 2.52 |
| FeO ^{Tc} | | 5.90 | 6.45 | 6.43 | 8.14 | 6.60 | 7.18 |
| MnO | | 0.16 | 0.17 | 0.16 | 0.21 | 0.16 | 0.19 |
| MgO | | 16.29 | 16.16 | 16.02 | 15.65 | 17.04 | 16.49 |
| CaO | | 21.44 | 21.09 | 20.96 | 19.84 | 20.77 | 20.26 |
| Na ₂ O | | 0.21 | 0.34 | 0.31 | 0.29 | 0.28 | 0.19 |
| Cr ₂ O ₃ | | 0.33 | 0.29 | 0.31 | 0.19 | 0.18 | 0.14 |
| Total | | 99.72 | 99.88 | 99.35 | 99.66 | 100.79 | 99.17 |
| Fe ^{3+d} | | 0.02 | 0.05 | 0.04 | 0.05 | 0.02 | 0.04 |
| Fe ^{2+d} | | 0.16 | 0.15 | 0.16 | 0.20 | 0.18 | 0.18 |
| En | | 47 | 46 | 46 | 45 | 48 | 47 |
| Fs | | 9 | 10 | 10 | 13 | 10 | 11 |
| Wo | | 44 | 43 | 43 | 41 | 42 | 42 |
| Mg# ^c | | 83 | 82 | 82 | 77 | 82 | 80 |
| Olivine | Identifier ^a | c | r | c | g | c | c |
| | SiO ₂ ^b | 38.77 | 38.92 | 40.25 | 38.14 | 38.81 | 38.85 |
| | TiO ₂ | b.d. | 0.04 | b.d. | 0.05 | b.d. | 0.02 |
| | Al ₂ O ₃ | b.d. | b.d. | 0.05 | b.d. | 0.04 | 0.04 |
| | FeO ^{Tc} | 19.33 | 20.88 | 15.62 | 24.37 | 20.42 | 19.90 |
| | MnO | 0.30 | 0.32 | 0.23 | 0.37 | 0.32 | 0.32 |
| | MgO | 41.23 | 40.48 | 44.41 | 36.69 | 40.27 | 40.27 |
| | CaO | 0.36 | 0.37 | 0.30 | 0.38 | 0.37 | 0.38 |
| | Total | 99.99 | 101.01 | 100.86 | 100.00 | 100.23 | 99.79 |
| | Fo | 78.9 | 77.3 | 83.3 | 72.6 | 77.6 | 78.0 |
| | Fa | 20.8 | 22.4 | 16.4 | 27.0 | 22.1 | 21.6 |
| Tp | 0.3 | 0.3 | 0.2 | 0.4 | 0.4 | 0.4 | |
| Mg# ^c | 79 | 78 | 84 | 73 | 78 | 78 | |

b.d. below detection level

^aIdentifier: *r* rim, *c* core, *g* groundmass, *i* inclusion

^bEMPA analysis (wt.% oxide)—University of Bristol

^cFeO^T is total Fe

^dFe ratio is calculated using the method of Schumacher (1997)

^eMg number 100×wt.%MgO/(MgO+FeO^T)

depth, we have assumed a crustal density of ~2,850 kg m⁻³ based on gravity studies in the Main Ethiopian Rift (e.g. Mahatsente et al. 1999). The calculated saturation depths are shallow: 0.2 to 1.4 km.

Trace element contents of melt inclusions (Table 4) are broadly similar to those of the host lavas with slightly elevated

incompatible elements and lower compatible elements, consistent with ~20 % crystallisation, i.e. the phenocryst content. Incompatible elements, e.g. Ba, are positively correlated with H₂O and negatively correlated with CO₂, despite a relatively small variation in all parameters (Fig. 6). The trace element content of the underlying lava (EA002) differs from the 2010

Table 4 Averaged melt inclusion major, trace and volatile analyses with host olivine analyses, and matrix glass majors and volatiles

| Sample | EA003 | | EA003 | | EA003 | | EA003 | | EA003 | | EA003b | EA003b | EA003 |
|-------------------------------------|---------|-------|---------|-------|---------|-------|---------|-------|---------|-------|--------|--------|--------|
| | Olivine | G | Olivine | H | Olivine | I | Olivine | J | Olivine | L | 3 | 6 | Matrix |
| <i>n</i> | 2 | 4 | 2 | 4 | 2 | 4 | 2 | 5 | 2 | 4 | | | 5 |
| SiO ₂ (wt%) ^a | 38.77 | 49.17 | 39.11 | 49.29 | 39.19 | 49.32 | 39.07 | 49.88 | 38.32 | 49.28 | | | 49.26 |
| TiO ₂ | 0.01 | 2.42 | 0.00 | 2.38 | 0.02 | 2.42 | 0.00 | 2.30 | 0.01 | 2.50 | | | 2.41 |
| Al ₂ O ₃ | 0.02 | 13.84 | 0.02 | 13.94 | 0.00 | 13.84 | 0.02 | 14.18 | 0.04 | 13.75 | | | 13.86 |
| FeO | 19.16 | 11.49 | 19.36 | 11.30 | 19.90 | 11.80 | 18.55 | 10.94 | 20.15 | 12.13 | | | 11.36 |
| MnO | 0.32 | 0.23 | 0.31 | 0.21 | 0.33 | 0.21 | 0.29 | 0.22 | 0.31 | 0.23 | | | 0.27 |
| MgO | 41.13 | 5.60 | 40.75 | 6.15 | 40.84 | 4.79 | 41.43 | 6.02 | 40.29 | 5.40 | | | 6.27 |
| CaO | 0.35 | 11.96 | 0.33 | 11.74 | 0.35 | 12.43 | 0.33 | 11.75 | 0.35 | 11.75 | | | 11.33 |
| Na ₂ O | 0.00 | 2.83 | 0.00 | 2.71 | 0.00 | 2.77 | 0.00 | 2.86 | 0.00 | 2.94 | | | 2.97 |
| K ₂ O | | 0.58 | | 0.55 | | 0.55 | | 0.57 | | 0.59 | | | 0.63 |
| P ₂ O ₅ | 0.00 | 0.51 | 0.02 | 0.39 | 0.02 | 0.36 | 0.00 | 0.38 | 0.00 | 0.39 | | | 0.37 |
| F | | b.d. | | b.d. | | b.d. | | b.d. | | b.d. | | | b.d. |
| Total | | 98.63 | | 98.66 | | 98.48 | | 99.09 | | 98.98 | | | 98.72 |
| Forsterite | 79.01 | | 78.69 | | 78.26 | | 79.68 | | 77.83 | | | | |
| Fayalite | 20.64 | | 20.97 | | 21.38 | | 20.00 | | 21.83 | | | | |
| Tephroite | 0.34 | | 0.34 | | 0.36 | | 0.32 | | 0.34 | | | | |
| Mg# ^b | 79.29 | | 78.96 | | 78.54 | | 79.93 | | 78.10 | | | | |
| SIMS (<i>n</i>) | | 2 | | 3 | | 3 | | 2 | | 1 | | | 2 |
| H ₂ O (ppm) ^c | | 1329 | | 867 | | 1118 | | 1035 | | 910 | | | 559 |
| uncertainty ^d | | 37 | | 24 | | 32 | | 34 | | 20 | | | 20 |
| CO ₂ (ppm) ^c | | 33 | | 194 | | 82 | | 124 | | 130 | | | <50 |
| uncertainty ^d | | 1 | | 6 | | 2 | | 4 | | 4 | | | |
| FTIR (<i>n</i>) | | | | | | 2 | | 2 | | | | | 2 |
| H ₂ O (ppm) ^e | | | | | | 2000 | | 1700 | | | | | 1700 |
| uncertainty ^f | | | | | | 400 | | 340 | | | | | 340 |
| CO ₂ (ppm) ^e | | | | | | 94 | | 136 | | | | | <50 |
| uncertainty ^f | | | | | | 33 | | 50 | | | | | |
| <i>n</i> | | | | | | | | 4 | | | 1 | 1 | 25 |
| SO ₂ (ppm) ^a | | | | | | | | 419 | | | 308 | 247 | 91 |
| sd (1σ) ^e | | | | | | | | 67 | | | | | |
| Cl (ppm) ^a | | | | | | | | 368 | | | 158 | 251 | 195 |
| sd (1σ) ^e | | | | | | | | 148 | | | | | |
| T (°C) ^g | | 1174 | | 1169 | | 1179 | | 1175 | | 1182 | | | |
| P (Mpa) ^h | | 7 | | 40 | | 16 | | 25 | | 27 | | | |
| Depth (km) ⁱ | | 0.2 | | 1.4 | | 0.6 | | 0.9 | | 0.9 | | | |
| <i>n</i> | | 2 | | 3 | | 3 | | 2 | | 1 | | | |
| Be (ppm) ^j | | 1 | | 1 | | 1 | | 1 | | 1 | | | |
| B | | 4 | | 4 | | 4 | | 4 | | 3 | | | |
| Sc | | 45 | | 45 | | 48 | | 45 | | 45 | | | |
| Sr | | 330 | | 334 | | 355 | | 327 | | 340 | | | |
| Y | | 41 | | 41 | | 43 | | 40 | | 40 | | | |
| Zr | | 221 | | 210 | | 218 | | 213 | | 219 | | | |
| Nb | | 38 | | 34 | | 36 | | 34 | | 39 | | | |
| Ba | | 166 | | 153 | | 164 | | 156 | | 174 | | | |
| La | | 33 | | 31 | | 35 | | 33 | | 32 | | | |
| Ce | | 65 | | 64 | | 70 | | 64 | | 65 | | | |
| Pr | | 8 | | 8 | | 8 | | 8 | | 8 | | | |

Table 4 (continued)

| Sample | EA003 | | EA003 | | EA003 | | EA003 | | EA003 | | EA003b | EA003b | EA003 |
|---------|---------|----|---------|----|---------|----|---------|----|---------|----|--------|--------|--------|
| | Olivine | G | Olivine | H | Olivine | I | Olivine | J | Olivine | L | | | |
| Host/MI | | | | | | | | | | | 3 | 6 | Matrix |
| Nd | | 26 | | 25 | | 27 | | 26 | | 25 | | | |
| Sm | | 8 | | 7 | | 8 | | 8 | | 8 | | | |
| Tb | | 1 | | 1 | | 1 | | 1 | | 1 | | | |
| Dy | | 6 | | 6 | | 7 | | 5 | | 6 | | | |
| Ho | | 1 | | 1 | | 1 | | 1 | | 1 | | | |
| Er | | 4 | | 4 | | 4 | | 4 | | 4 | | | |
| Yb | | 3 | | 3 | | 3 | | 3 | | 3 | | | |
| Lu | | 0 | | 1 | | 0 | | 1 | | 1 | | | |
| Hf | | 4 | | 4 | | 4 | | 4 | | 4 | | | |
| Ta | | 2 | | 2 | | 2 | | 2 | | 2 | | | |
| Th | | 3 | | 4 | | 4 | | 4 | | 3 | | | |
| U | | 1 | | 1 | | 1 | | 1 | | 1 | | | |

n number of analyses, *b.d.* below detection level, *blank* space no analysis, *host* phenocryst hosting the inclusion, *identifier* melt inclusion

^a Averaged major element analysis—EMPA, University of Bristol

^b Mg number $100 \times \text{wt.}\% \text{ MgO}/(\text{MgO} + \text{FeO}^{\text{T}})$

^c Averaged SIMS analysis, University of Edinburgh

^d Average uncertainty as determined by full propagation of counting statistics, instrument background and calibration working curve

^e FTIR, University of Bristol

^f IR propagated uncertainty—see text for error source

^g Temperature in degrees Celsius using the method of Putirka (2008). Calibration error ± 45 °C,

^h Pressure in MPa using the method of Newman and Lowenstern

ⁱ Depth calculated from P assuming a crustal density of $\sim 2,850 \text{ kgm}^{-3}$. Depth is depth below surface.

^j Trace elements determined by SIMS analysis at the University of Edinburgh

lavas, most noticeable in the elevated levels of incompatible Ba which may reflect the greater crystallinity of this sample.

K α X-ray mapping of an olivine phenocryst from EA001 indicates homogeneity throughout the crystal for major elements such as Fe (Fig. 3h). However, feint concentric, oscillatory zoning is visible in phosphorous (Fig. 3g).

Integration of ground observations, satellite imagery and petrology

Ground observations and satellite imagery

In a location as remote as Erta Ale, eruptions can occur unnoticed and unrecorded. The November 2010 eruption was short lived, which is typical of recent eruptions in Afar (e.g. Ferguson et al. 2010; Wright et al. 2006), and ordinarily, the brevity would not allow scientists sufficient time to travel to the eruption site to make observations. However, from the interpretation of the SEVERI features of the radiance time series, together with serendipitous ground observations, we can make inferences about the eruption chronology.

The SEVERI data suggest the first thermal anomaly period occurred between 11 November and 14 November (Fig. 4), and records overflows onto the southern pit floor only. By the end of the first period, the pit floor had been covered with fresh lava flows, but the lake level was still low enough that the rim of the pit obscured it from view by SEVERI. Ground observations from 11 November confirm that the southern pit was still >20 m deep, comparable to its state 6 months earlier in February 2010 (Fig. 2a, b). However, by 14 November, the base of the pit was covered in fresh lava (J. Wilkinson, personal communication, December 2010). There then followed a hiatus of overflows, up until the start of the second thermal anomaly period, as seen by the lack of excess radiation (Fig. 4).

It was during this period of quiescence that seismic activity occurred in the Gulf of Aden [14–17 November—European-Mediterranean Seismological Centre (EMSC 2010)] and around the town of Chiro (formerly Asebe Terferi) at the northern end of the Main Ethiopian Rift. Disturbance was also reported in the Danakil region with the opening of large sinkholes and unusually high groundwater levels.

Table 5 Calculated thermometry

| | Matrix glass thermometry | | | | Melt inclusion thermometry | | |
|-----------------------------------------------|--------------------------|--------------------------------|------------------------|----------------------------|----------------------------|------------------------------------------|-------|
| | Mineral | Plagioclase/liquid (rim/glass) | CPX/liquid (rim/glass) | Olivine/liquid (rim/glass) | | Olivine/liquid (corrected olivine/glass) | |
| Method | Putirka (2008) | Putirka (1996) | Putirka (2008) | Beattie (1993) | Putirka (2007) | Beattie (1993) | |
| Calibration error | ±36 °C | ±52 °C | ±45 °C | ±44 °C | ±45 °C | ±44 °C | |
| Temperature, °C | 1,176 | 1,165 | 1,158 | 1,157 | 1,126 | 1,132 | |
| | 1,180 | 1,169 | 1,157 | 1,157 | 1,148 | 1,148 | |
| | 1,176 | 1,151 | 1,158 | 1,157 | 1,094 | 1,104 | |
| | 1,173 | 1,148 | 1,157 | 1,157 | 1,140 | 1,143 | |
| | 1,180 | 1,167 | 1,157 | 1,157 | 1,121 | 1,129 | |
| | 1,171 | 1,175 | 1,157 | 1,157 | | | |
| | 1,178 | 1,169 | 1,152 | 1,157 | | | |
| | | | 1,167 | 1,151 | | | |
| | | | 1,157 | 1,155 | | | |
| | | | 1,170 | 1,157 | | | |
| | | | 1,170 | 1,155 | | | |
| | | | 1,162 | 1,155 | | | |
| | | | | 1,153 | | | |
| | | | | 1,153 | | | |
| | | | | 1,156 | | | |
| | | | | 1,157 | | | |
| | | | | 1,155 | | | |
| | | | 1,155 | | | | |
| All temperatures calculated from sample EA003 | Mean | 1,176 | 1,164 | 1,155 | 1,157 | 1,126 | 1,131 |

The field team arrived at ~1600 hours UTC on 21 November when the second phase of the eruption was well underway, and the southern pit had filled. SEVERI imaging suggests this second phase of activity began during 19 November, which indicates a rapid infilling of the southern pit between the 19th and 21st (Figs. 2 and 4). Assuming little or no activity between 15 and 19 November, a flow rate of approximately $2 \text{ m}^3 \text{ s}^{-1}$ would be required to fill the area of the pit between 19 and 21 November (53 h). Oppenheimer and Francis (1997) estimated an average magma discharge rate (MDR) of $\sim 400 \text{ kg s}^{-1}$ for February 1972–March 1973. Assuming the same density for comparison ($2,700 \text{ kg m}^{-3}$), the calculated MDR for 19–21 November is $\sim 5,600 \text{ kg s}^{-1}$. The first overflow outside of the southern pit onto the main crater floor occurred at ~1750 hours UTC (Fig. 3a). Throughout the eruption, the lake was surrounded by a scoria ring cone which continued to build, similar to that observed in 1973 (Tazieff 1973). Overflows continued at approximately 2-h intervals until ~1430 hours UTC on 22 November (Supplementary Video 1).

For the remainder of the ground observations, the lake was contained within the scoria ring, which had grown to

~4 m high by 0300 hours UTC on 23 November. A 20-min cycle followed, with lava lake levels rising and falling by >4 m, during which, peak levels were marked by Strombolian activity. The northern part of the ring suffered a partial collapse on the morning of 23 November, which corresponds to a sharp peak at 0400 hours UTC in the SEVERI imaging (Fig. 4). Periodically, incandescent blue-green gas jets were observed similar in description to gas flames reported in January 2003, assumed to be SO_2 (Vetsch et al. 2003). The northern pit also showed signs of activity with fresh lava flows erupted during the night of 21 November.

After the field team departed on 23 November, the eruption continued, with new overflows covering over the sampled flows, and nearly reaching the western rim of the caldera (Fig. 1; J. Hammond and J. Wilkinson, personal communication). The spacing between successive overflows became long enough that periods of sustained radiance can be identified, indicating that the lava lake had gained sufficient height to come into view of the sensor. SEVERI indicates lake activity persisted with sparse superimposed overflows for 7 days, followed by a period of sustained lake

activity with no overflows for 6 days, and within a further 4 days, after 30 November, the lake signal disappeared, indicating a drop in lake level and occultation of the lake by the rim once again. Cloud cover prevents us determining the exact end of the eruption, but activity was confirmed to have ceased prior to 15 December (J. Wilkinson, personal communication, December 2010). In summary, the pattern appears to be (1) first period of lake level rise, (2) hiatus/drop in lake level, (3) lake level rise including lava overflows into the southern pit, (4) lake level stabilisation at high stand including lava overflows into the main crater and (5) lake level drop. The estimated total volume of both the erupted surface lava flows and the volume of lava required to fill the pit from the previous level is $\sim 0.006 \text{ km}^3$, based on an estimated pit depth of 20 m.

Thermometry

There is good agreement between temperatures determined in February 2001 by Burgi et al. (2002) using thermocouples and pyrometers (1,145–1,187 °C), and the petrological estimates reported here (1,094–1,180 °C). The temperatures are within error indicating a temperature for the system of $\sim 1,150 \text{ °C}$, although there are likely to be some fluctuations within the conduit caused by magma circulation between magma storage, the conduit and the lake itself (Harris et al. 2005). Temperatures determined by Le Guern et al. (1979) in December 1971, January 1973 and 1974 provided a range of 1,100 °C through 1,210 °C. The Le Guern field team directly inserted thermocouples into active hornitos, which may account for the differences between their study and the study of Burgi et al. (2002).

Volatiles

The petrology indicates that crystallisation is taking place in the upper $\sim 1.5 \text{ km}$ of the conduit. The highest H_2O content measured in the melt inclusions is low, $>0.13 \text{ wt.}\%$, lower than the water content proposed for a typical alkali basalt ($\sim 0.5 \text{ wt.}\%$; e.g. Lowenstern and Mahood 1991). The low water values in the melt inclusions are very similar to basaltic melt inclusions from Hawaii (Fig. 5a, Hauri 2002), but significantly lower than MORB (e.g. Pineau and Javoy 1994), Piton de la Fournaise, Réunion (Bureau et al. 1998) and Iceland (Nichols et al. 2002; Nichols and Wysoczanski 2007), which yield H_2O contents up to 0.9 wt.%. Low H_2O and CO_2 content can result from leakage, e.g. through cracks, and diffusive loss can occur through the host olivine. However, no cracks or bubbles were present in any of the inclusions studied. The positive correlations between trace elements and volatiles (Fig. 6) could not be preserved if significant H_2O had diffused out of the inclusions as H_2O , CO_2 and trace elements have very different diffusivities through olivine. The sole exception is melt inclusion L which has a slightly higher Ba than other melt inclusions (Fig. 6) and may represent entrapment of a slightly different melt composition. The overall trajectory of melt inclusion volatiles, namely, the large range in CO_2 with little range in H_2O (Fig. 5a), suggests that, although the magma became extensively degassed during ascent, the original magmatic H_2O content was not significantly higher than 0.15 wt.%. There are several lines of evidence that the Erta Ale magma was volatile-saturated prior to eruption. Our CO_2 – H_2O data define an array which is oblique to the isobars, consistent with decompression-driven degassing (Fig. 5a, b). However, the

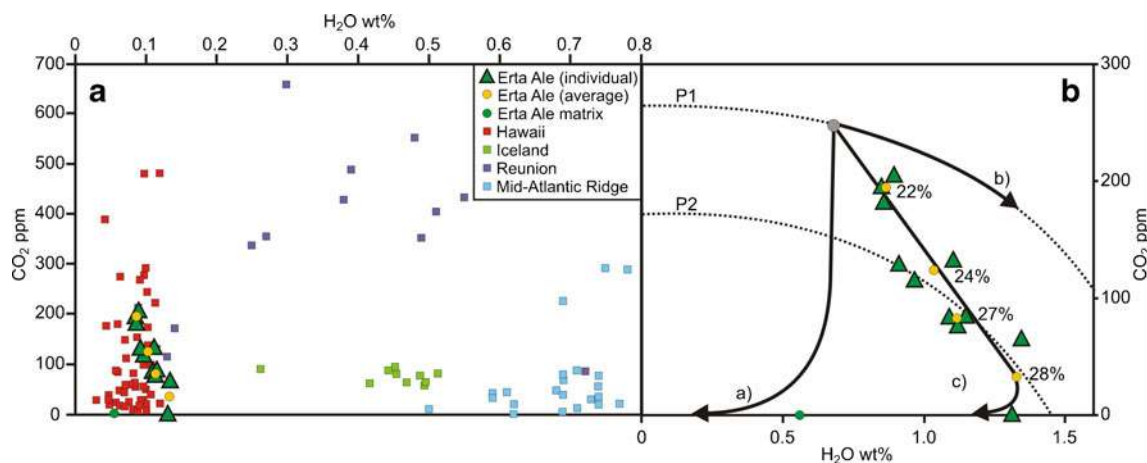


Fig. 5 **a** Plot of CO_2 vs. H_2O in melt inclusion and matrix glasses compared to other basaltic systems. Note broad agreement between Erta Ale (green triangles and yellow circles) and Hawaii (Hauri 2002). **b** Close-up of the data from Erta Ale (same symbols as **a**) indicating possible volatile evolution paths in melt inclusions (solid lines), based on Blundy and Cashman (2008). Dotted lines indicate schematic isobars for pressure $P_1 > P_2$ (their exact positions are poorly constrained at

these low pressures). Path *a* indicates vapour-saturated decompression without crystallisation, path *b* indicates isobaric vapour-saturated crystallisation and path *c* indicates vapour-saturated decompression crystallisation. Percentages in *c* indicate crystallisation. Path *c* best describes the Erta Ale data. Values indicate approximate percentage of crystallisation calculated from the Ba values of averaged MI, normalised to whole-rock Ba

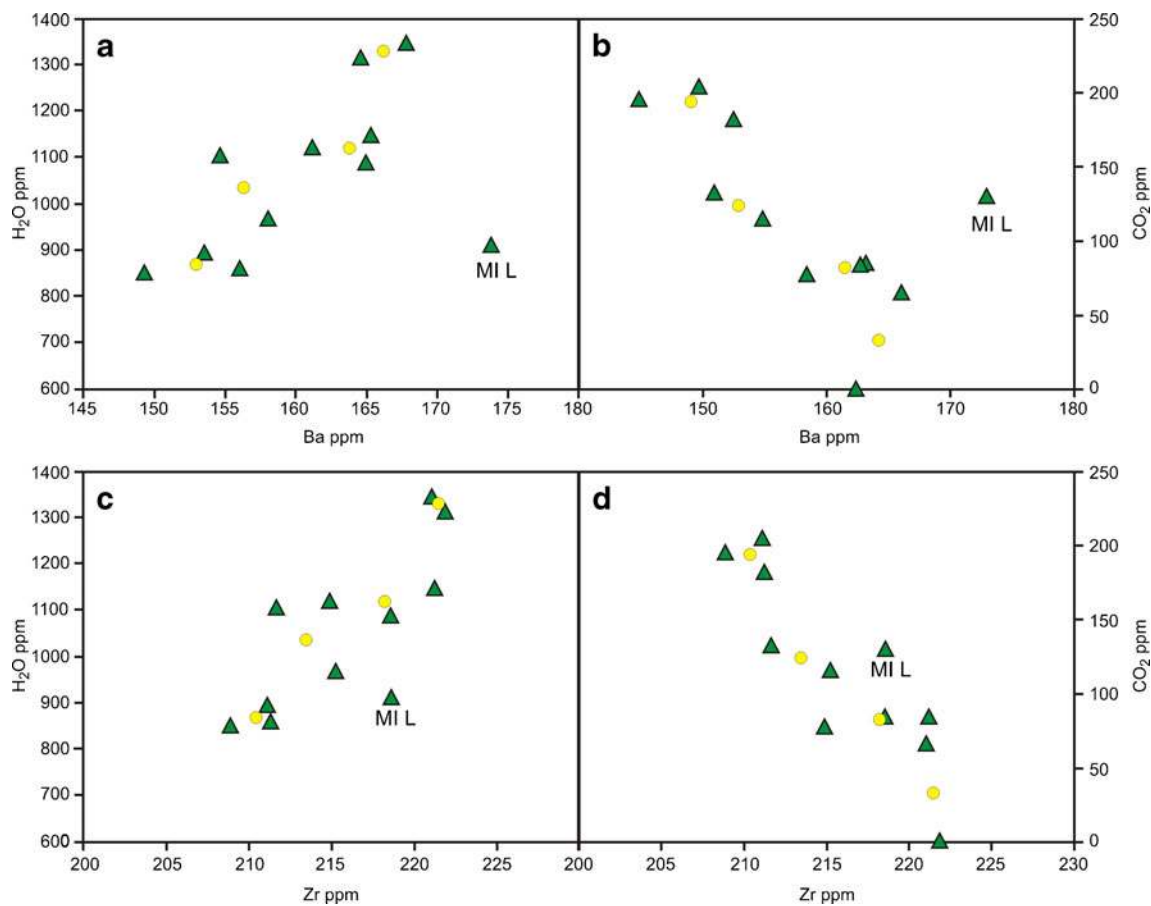


Fig. 6 Melt inclusion analyses of H₂O (**a**, **c**) and CO₂ (**b**, **d**) plotted against concentrations of the incompatible elements Ba and Zr. These plots suggest that the November 2010 lavas experienced vapour-saturated crystallisation, as both Ba and Zr are positively correlated with H₂O and negatively correlated with CO₂. *Green triangles* show

individual SIMS analyses; *yellow circles* indicate the averaged analysis for each melt inclusion studied. Melt inclusion (MI) L lies distinct from the main melt inclusion trend and may represent the presence of a slightly different magma composition within the system

negative slope of the array cannot be ascribed to degassing alone, which would produce a steep positive (sub-vertical) array, due to the much lower solubility of CO₂ compared to H₂O. The positive correlation of an incompatible element, such as Ba or Zr, with H₂O (Fig. 6), and negative correlation with CO₂ are consistent with vapour-saturated crystallisation (Blundy and Cashman 2008). A possible explanation is that crystallisation occurred concomitantly with decompression in Erta Ale magmas. Simple mass balance calculations for EA003 indicate ~19 vol% crystallisation is required to obtain the melt inclusion composition from the bulk rock, which is comparable to the modal volume for this sample of ~18 vol%, obtained by point counting. Note that if the inclusions had lost water by diffusion, the H₂O (which diffuses more rapidly than CO₂) would be displaced to low values at a given CO₂ content, which is not observed (Fig. 5a).

The conclusion that Erta Ale magmas were volatile-saturated at shallow levels allows us to estimate, using VolatileCalc (Newman and Lowenstern 2002), the composition of the coexisting exsolved gas for comparison to previous

measurements from Erta Ale. The estimate for exsolved gas in November 2010 is 0.2–2.9 mol% H₂O and 97.1–99.8 mol% CO₂, i.e. molar H₂O/CO₂ ratios of 0.002 to 0.03. There is appreciable uncertainty in this estimate due to the paucity of experimental data on basalts at low pressures. Nonetheless, these estimated volatile compositions are significantly more H₂O poor than those determined by Gerlach (1980) and Sawyer et al. (2008) during passive degassing of the Erta Ale lava lake, who give molar H₂O/CO₂ ratios of 4–7 and 25, respectively (Table 6). As CO₂ is considerably less soluble in basalt than H₂O, the elevated H₂O/CO₂ suggests that passive degassing involves volatiles released at shallower depths than those at which melt inclusions were trapped. One way to evaluate this hypothesis is to calculate the composition of the total gas released by the ascending magma from the difference between melt inclusion and matrix glass volatile contents. This is, in effect, an integration of the gas released from the magma as it ascends to the surface. As the matrix glass has CO₂ contents below detection, we assume all CO₂ has been lost by degassing making our

Table 6 Calculated molar gas ratios

| | This study | | | | Sawyer et al. (2008) | | Gerlach (1980) | | | |
|----------------------------------------|----------------------|-----|---------------------|-----|----------------------|-----|-------------------|-------------------|-------------------|-------------------|
| | Average ^a | sd | EA003J ^b | sd | 2005 | sd | 1974 ^c | 1973 ^d | 1973 ^d | 1971 ^e |
| H ₂ O/CO ₂ (mol) | 10.7 | 7.2 | 9.4 | 1.6 | 24.8 | 0.8 | 6.6 | 3.8 | 3.7 | 3.9 |
| CO ₂ /SO ₂ | 0.7 | 0.5 | 0.5 | 0.1 | 1.5 | 0.1 | 1.6 | 2.7 | 4 | 2 |
| SO ₂ /Cl | 1.9 | 3.1 | 1.0 | 0.6 | 12.4 | 0.2 | 18.6 | | | |
| H ₂ O/SO ₂ | 7.1 | 3.8 | 5.0 | 0.8 | 38 | 3 | 10.4 | 10.4 | 14.5 | 7.9 |

^a Average from this study, calculated using melt inclusion minus matrix analysis for each species

^b Example of an individual melt inclusion, calculated using melt inclusion minus matrix analysis for each species

^c Ratios from restored gas analysis (Gerlach 1980) (gases originally collected in 1974 from hornitos by Giggenbach and Le Guern)

^d Ratios from restored gas analysis (Gerlach 1980) (1973 gases originally collected from a homito by Le Guern)

^e Ratios from restored gas analysis (Gerlach 1980) (1971 samples originally collected by Tazieff)

H₂O/CO₂ estimates maxima. Our calculated values for molar H₂O/CO₂ from individual melt inclusions lie in the range 4–57 with an average for the entire population of 11±7. These H₂O/CO₂ ratios fall within the range determined by Sawyer et al. (2008) and Gerlach (1980). This suggests that the composition of the gas released from the magma is consistent, quantitatively, with exsolution of pre-eruptive volatiles contained within the magma; if a significant population of bubbles of deeper, magmatic gas with elevated CO₂/H₂O was present in the magma prior to ascent, this would reduce the H₂O/CO₂ ratio of the gas below the values observed by Sawyer et al. (2008) and Gerlach (1980).

The calculated molar SO₂/Cl ratio of the released gas is in the range 1.0–2.0 (Table 6) compared to 12–19 measured in field studies (Gerlach 1980; Sawyer et al. 2008). As chlorine is the last volatile species to be exsolved from magma, the SO₂/Cl ratio is a sensitive indicator of degassing depth (Lesne et al. 2011): higher ratios denote shallower degassing. Our low SO₂/Cl ratios are consistent with complete degassing upon eruption in November 2010. Conversely, the lava lake gas measurement of Gerlach (1980) and Sawyer et al. (2008), which were made at a time when the lava was contained within the pit and not overflowing into the main crater, likely records a slightly deeper level of degassing, probably due to circulation within the conduit, giving rise to higher SO₂/Cl ratios. These small changes in degassing depth will not have significant effect on the H₂O/CO₂ ratios, as almost all CO₂ is lost prior to the onset of Cl degassing (Lesne et al. 2011). A schematic illustration of the Erta Ale shallow plumbing system that is consistent with the observed differences in gas composition between eruptive and non-eruptive (passive) degassing episodes is shown in Fig. 7.

The difference in SO₂ contents of melt inclusions and matrix glass is in the range 160 to 330 ppm (Table 4).

Assuming that the November 2010 magma had a similar composition to that in the lava lake in 2005 when studied by Sawyer et al. (2008), we calculate the total magma flux through the conduit required to sustain their observed SO₂ flux (0.69±0.17 kg s⁻¹) to be in the range 2,090±520 to 4,310±1,060 kg s⁻¹. A broadly similar magma flux, calculated in the same way, can sustain the range of CO₂ fluxes measured by Sawyer et al. (2008). However, a higher flux, by a factor of two, is required to sustain the observed H₂O flux. This mismatch may be rooted in the combined uncertainties on the analytical and gas measurement data, or reflect, as suggested above, small differences in the degassing depths between and during eruptions. Sawyer et al. (2008) noted that the H₂O in the volcanic plume had significantly increased in the 30 years since Gerlach's (1980) work, and suggested this may be related to volatile depletion of the deep source magma and/or to fractional magma degassing. Alternatively, variation in the H₂O content of Erta Ale gases may reflect systematic changes in the depth within the conduit at which gases are extracted. In any case, our calculations lend support to the idea that the observed gas flux can be provided by near-complete degassing of magma passing through the shallow conduit system at rates of ~3,000–7,000 kg s⁻¹. It does not appear that any substantial additional source of gas, i.e. gas-fluxing, is required to account for the field measurements of gas flux at Erta Ale.

The Erta Ale lavas show a high vesicularity (up to ~60 %), which may initially seem surprising given the low volatile contents indicated by the melt inclusions. Using the ideal gas law, the average value for lost H₂O of 450 ppm (i.e. melt inclusion minus groundmass), a temperature of 1,150 °C, standard atmospheric pressure and an assumed density for basalt of 2,700 kg m⁻³ (e.g. Oppenheimer and Francis 1997), a gas volume of 2.92×10⁻³ m³ is obtained, ~8 times more gas than melt. This indicates that if 10 % degassing were to take

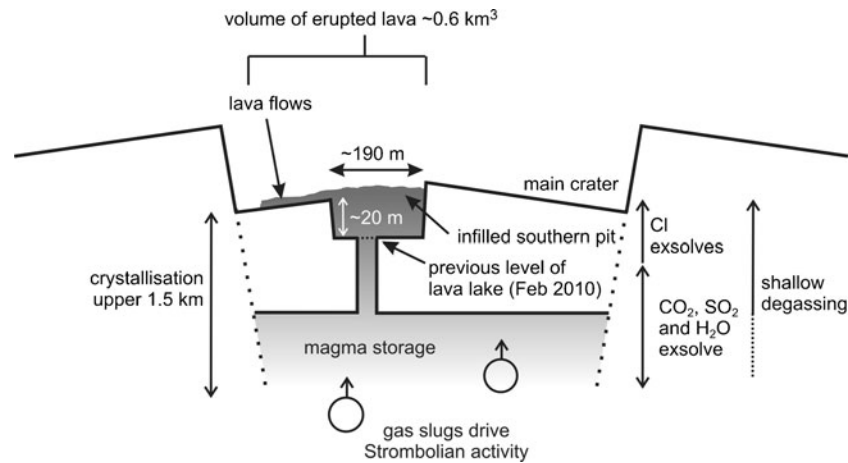


Fig. 7 Schematic of the Erta Ale shallow plumbing system in November 2010 based on integrated ground and satellite observations and petrology (not to scale). The arrows on the right hand side illustrate how gas extraction from different depths influences gas composition, with elevated Cl characteristic of very shallow degassing. Passive

degassing does not appear to require an additional source of gas to explain the measured gas chemistry; it is sufficient that magma ascends from the storage region to the lake itself releasing its volatiles en-route. However, it is possible that vigorous Strombolian activity is triggered by the ascent of large bubbles from depth as shown schematically

place, ~40 % vesicularity would result, and 20 % degassing would result in ~60 % vesicularity. Thus, releasing <448 ppm gas at, or close to, the surface at the eruption temperature is sufficient to generate the observed high vesicularities. Melt inclusion volatile data are also not suggestive of the presence of significant pre-eruptive bubbles in the magma during passive degassing episodes (see above). However, we cannot rule out the possibility that an influx of additional gas drove the Strombolian activity observed in 2010. We have no field measurements of this degassing episode with which to test our hypothesis, but it does seem likely that an additional gas source was required to sustain the observed eruptive vigour.

During eruption, the viscosity of the lava appeared to be very low (Supplementary Video 1). The calculated viscosity of the melt at eruption temperature using the model of Giordano et al. (2008) is 70 Pas. The small fraction of crystals (~18 vol% in EA003) is unlikely to have had any major impact on the viscosity (Caricchi et al. 2007). However, the vesicularity would have had a greater effect. The vesicles observed in the Erta Ale samples are highly elongate, which would have resulted in a lowering of viscosity, whilst spherical vesicles would instead have acted like phenocrysts to raise the viscosity (Llewellyn and Manga 2005). Consequently, the calculated viscosity of the vesicular magma is reduced to 5 Pas (Pal 2003) or 15 Pas (Llewellyn and Manga 2005).

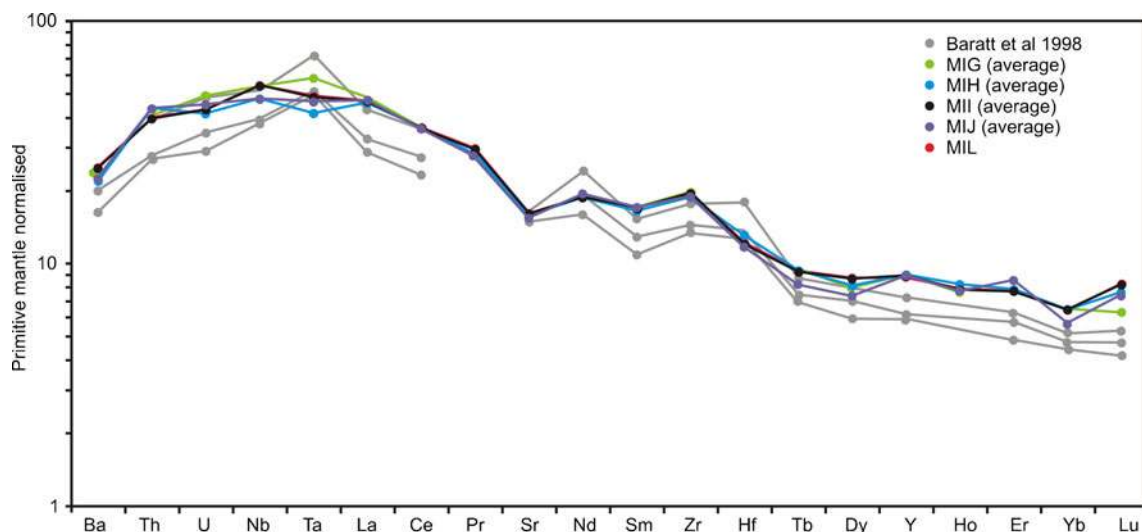


Fig. 8 Trace element compositions normalised to primitive mantle (Sun and McDonough 1989) of melt inclusions, with whole rock data from an Erta Ale basalt of Barrat et al. (1998) for comparison. The

broadly similar patterns are consistent with crystallisation of an olivine-dominated phenocryst assemblage. The small negative Sr anomaly is consistent with plagioclase crystallisation

Geochemistry

A key question is whether the geochemistry of the 2010 lavas is sufficiently different from those of earlier Erta Ale lavas to indicate that recharge of the magma system occurred subsequent to 1973. We have already shown that the 1973 lavas appear to be texturally and chemically distinct from those of 2010. However, these differences can be readily reconciled with a slightly increased degree of fractionation of EA002, as evinced by higher contents of incompatible elements, and lower temperatures as suggested by their more crystalline, microlite-rich texture. Overall, however, the 1973 and 2010 lavas are sufficiently similar to each other and within the range of Erta Ale Range lavas that it seems unlikely that any recharge of the system since 1973 involved a truly distinct magma type. Nonetheless, the renewal of activity, the reduction in differentiation and crystallinity strongly suggest that the sub-volcanic reservoir was refilled by hotter, compositionally similar basaltic magma.

Trace element systematics

Trace elements concentrations normalised to primitive mantle (Sun and McDonough 1989) are plotted in Fig. 8. Whole rock samples from Barrat et al. (1998) are shown for comparison. The melt inclusions have a similar overall pattern to the whole rocks, but are displaced to the high concentration end of the whole-rock range, consistent with a modest amount of crystallisation (~20 %) of trace element poor phenocrysts. The small negative anomaly for Sr, in both melt inclusions and whole rocks, is consistent with crystallisation of plagioclase. The presence of plagioclase inclusions in both cpx and olivine crystals indicates plagioclase was already crystallising when melt inclusions were entrapped in olivine. Europium, which also partitions strongly into plagioclase, was not measured in the melt inclusions due to the large isobaric interference of BaO on Eu at the mass resolution used for trace element analyses.

The relationship between the whole rocks and the melt inclusions is further illustrated using log–log plots in Fig. 9. The melt inclusions define linear trends that extend away from the 2010 whole rocks along vectors consistent with ~20 % crystallisation of an olivine-dominated assemblage with plagioclase and cpx. The range in trace element contents of the suite of melt inclusions records continued crystallisation of the same assemblage. The correlations between incompatible elements and volatile species (Fig. 6) suggest that this crystallisation occurred concomitantly with degassing. The subtle geochemical differences between the 2010 lavas and those of the lava floor are suggestive of magma refill of slightly different composition, although there is insufficient data to fully evaluate this possibility.

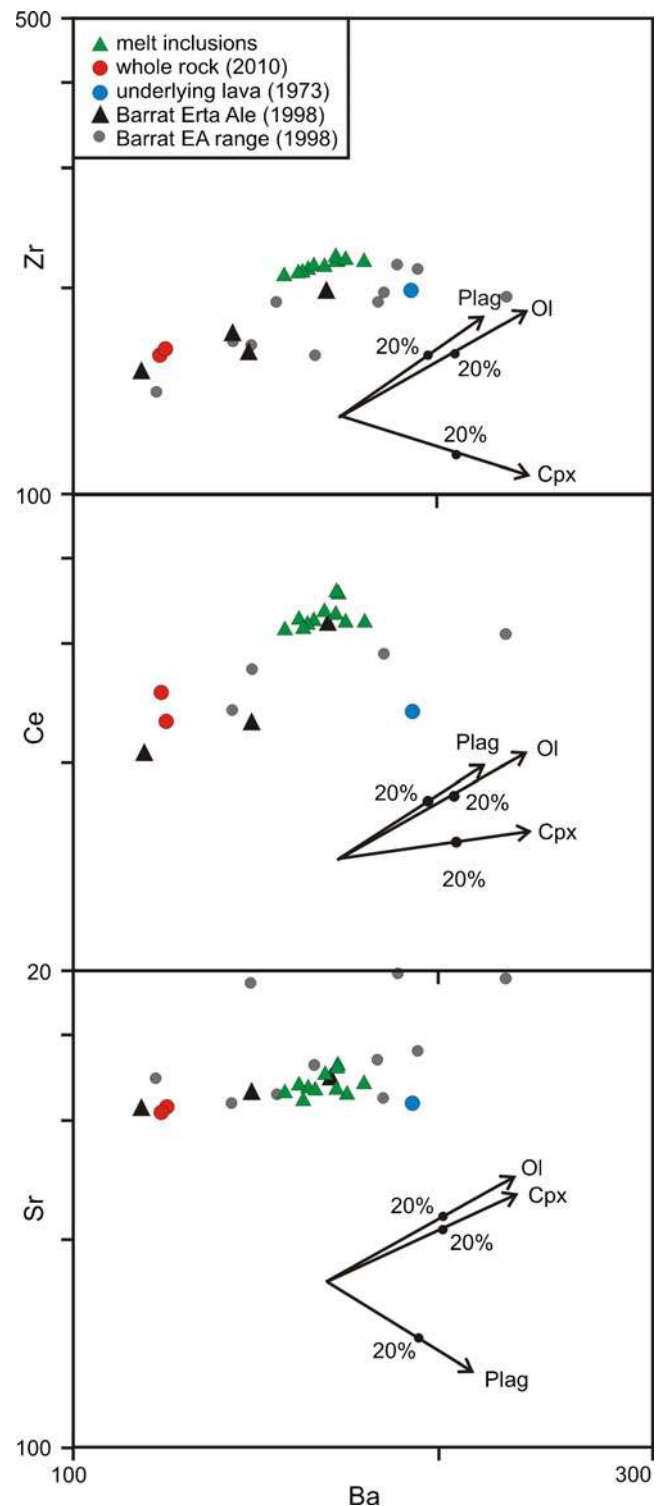


Fig. 9 Log–log trace element plots for individual melt inclusion analyses and whole rock. Vectors show the effect of fractionation of plagioclase, clinopyroxene and olivine using partition coefficients from Rollinson (1993). The filled circles denote 20 wt.% fractionation. Data from Barrat et al. (1998) from both the Erta Ale volcano and the Erta Ale range has been included for comparison

Magmatic timescales

K α X-ray mapping revealed phosphorous zoning in the olivines, which was not apparent for other elements, e.g. Fe (Fig. 3h). Phosphorous diffuses extremely slowly compared to Fe–Mg and Ca in olivine (Milman-Barris et al. 2008; Spandler and O'Neill 2010). Hence, the P zoning is preserved, whilst Fe–Mg and Ca are homogenised during residence in hot magma. An estimate of the minimum time it would take to homogenise the crystal with respect to Fe–Mg and Ca at magmatic temperatures can be obtained from the characteristic diffusion length ($x=(Dt)^{1/2}$; where x =distance, D =diffusivity, t =time) of each element of interest. Diffusion coefficients for Ca and Fe–Mg, parallel to the c -axis, were calculated using the models of Coogan et al. (2005), Dohmen et al. (2007) and Dohmen and Chakraborty (2007) at a magmatic temperature of 1,170 °C and an oxygen fugacity equivalent to the QFM buffer. For a typical 200- μ m olivine crystal, Fe–Mg would have homogenised in approximately 0.2 years, and Ca in 10 years, providing a minimum estimate for the residence time of a crystal within this magma. Phosphorous diffusion rates have not been constrained, but are at least two orders of magnitude slower than other major cations (Spandler and O'Neill 2010). Studies of experimental and natural olivines have shown P and Cr to be correlated (Milman-Barris et al. 2008). Cr diffusion coefficients (Ito and Ganguly 2006) were therefore used to give an indication of the minimum timescales required to eradicate the P zoning. This gives a minimum timescale of ~94 years for homogenisation of P within a typical 200- μ m olivine crystal, as modelled here. As P is not homogenous in the studied olivines, this timescale provides an upper limit for residence of this crystal. Although crystals can be retained in the sub-volcanic system following an eruptive episode, it is considered that this is unlikely as the texture and appearance of crystals in the 2010 samples (EA001 and 3) are very different from the underlying lava (EA002) from the previous over-spill (compare Fig. 3e, f). The last observed eruptive episode at Erta Ale was in 1973. The fact that the estimated timescales are of the order of decades, a period comparable to that elapsed since Erta Ale last erupted, is consistent with our earlier inferences that the magma system was recharged by a new pulse of hotter magma subsequent to 1973 (refer to Supplementary Table 5), we think these eruptive episodes are sufficiently infrequent that the period between the eruptions acts as an upper bound and therefore suggest that the crystal residence time was between ~10 and ~37 years.

Conclusions

We present an integrated field, satellite and petrological study of the November 2010 eruption of the Erta Ale volcano. The

timeline of this small, but rare, eruption has been reconstructed from a combination of ground observations and SEVERI imaging. Two phases occurred, beginning on 11 and 19 November 2010. Pristine melt inclusions have shown the Erta Ale magma to be relatively dry (<0.15 wt.% H₂O), although several petrological lines of evidence suggest the magma was volatile-saturated prior to eruption. The low volatile contents within the melt inclusions are sufficient at eruption temperature and low pressure, to account for the vesicularity of the erupted lava. The eruption and overflow of magma from the lava lake in November 2010 facilitated almost complete magma degassing. The calculated composition of the released gas is broadly consistent with measured passive emissions of volcanic gas from the Erta Ale lava lake, although the higher measured SO₂/Cl ratios suggests that degassing during non-eruptive episodes did not proceed to the same extent as it did during the 2010 eruption. Coupled trace and volatile element systematics indicate that crystallisation took place at shallow levels, in the top ~1.5 km of the conduit, largely in response to degassing. We tentatively conclude that slightly hotter, but broadly similar, magma was injected into the magmatic system after 1973, and that typical phenocryst residence times indicated by phenocrysts in the 2010 samples were between ~10 and 37 years. The 2010 samples are shown to be quite distinct from the underlying lava from the previous over-spills in 1973.

The November 2010 eruption was coincident with a seismic swarm in the Gulf of Aden; increased activity in 2005 was also noted to be coincident with the 2005 volcano-seismic crisis in the Manda-Hararo magmatic rift segment. It is possible that Erta Ale is particularly sensitive to tectonic activity in the region, but future monitoring will be required to confirm this.

Acknowledgments This research was funded by the Natural Environmental Research Council, Afar Rift Consortium grant NE/F007604/1. K.S. was supported by a NERC Post-doctoral Research Fellowship (NE/G0129X/1). The authors acknowledge the generous support of the University of Addis Ababa with fieldwork arrangements, and the Afar Regional Government for invaluable assistance. We thank N. Marsh and R. Kelly for assistance with XRF at the University of Leicester, R. Hinton with the SIMS at the University of Edinburgh and J. Hammond for the GPS track of the final emplaced lava flow (February 2011). J. Wilkinson is thanked for sharing his observations during and post-eruption. T. Rooney provided some helpful comments on an earlier version of the manuscript. The manuscript was also improved by the comments of two anonymous reviewers.

References

- Ayele A, Jacques E, Kassim M, Kidane T, Omar A, Tait S, Nercessian A, de Chabaliere J, King G (2007) The volcano-seismic crisis in Afar, Ethiopia starting September 2005. *Earth Planet Sci Lett* 255 (1–2):177–187

- Barrat JA, Fourcade S, Jahn BM, Cheminee JL, Capdevila R (1998) Isotope (Sr, Nd, Pb, O) and trace-element geochemistry of volcanics from the Erta Ale range (Ethiopia). *J Volcanol Geotherm Res* 80(1–2):85–100
- Barberi F, Varet J (1970) The Erta Ale volcanic range (Danakil depression, northern Afar, Ethiopia). *Bull Volcanol* 34(4):848–917
- Barberi F, Santacroce R, Varet J (1974) Silicic peralkaline volcanic rocks of the Afar depression (Ethiopia). *Bull Volcanol* 38(2):755–790
- Barberi F, Varet J (1977) Volcanism of Afar—small-scale plate tectonic implications. *Geol Soc Am Bull* 88(9):1251–1266
- Bardintzeff J, Gaudru H (2004) 11/2004 (BGVN 29:11) Bulletin of the Global Volcanism Network. Smithsonian Institute, Global Volcanism Program. www.si.edu. Accessed Jan 2011
- Beattie P (1993) Olivine-melt and orthopyroxene-melt equilibria. *Contrib Mineral Petrol* 115(1):103–111
- Bizouard H, Barberi F, Varet J (1980) Mineralogy and petrology of Erta Ale and Boina volcanic series, Afar Rift, Ethiopia. *J Petrol* 21(2):401–436
- Blundy J, Cashman K (2008) Petrologic reconstruction of magmatic system variables and processes. In: Putirka KD, Tepley FJ (eds) *Minerals, inclusions and volcanic processes*. Mineralogical Society of America, Chantilly, pp 179–239
- Bureau H, Pineau F, Métrich N, Semet MP, Javoy M (1998) A melt and fluid inclusion study of the gas phase at Piton de la Fournaise volcano (Réunion Island). *Chem Geol* 147(1–2):115–130
- Burgi P-Y, Caillet M, Haefeli S (2002) Field temperature measurements at Erta'Ale Lava Lake, Ethiopia. *Bull Volcanol* 64(7):472–485
- Caricchi L, Burlini L, Ulmer P, Gerya T, Vassalli M, Papale P (2007) Non-Newtonian rheology of crystal-bearing magmas and implications for magma ascent dynamics. *Earth Planet Sci Lett* 264(3–4):402–419
- Coogan LA, Hain A, Stahl S, Chakraborty S (2005) Experimental determination of the diffusion coefficient for calcium in olivine between 900°C and 1500°C. *Geochim Cosmochim Acta* 69(14):3683–3694
- Dainelli G, Marinelli O (1907) Vulcani attivi della Danalia. *Riv Geog Ital* 13:261–270
- Davies AG, Keszthelyi LP, Harris AJL (2010) The thermal signature of volcanic eruptions on Io and Earth. *J Volcanol Geotherm Res* 194(4):75–99
- Dixon JE, Stolper E, Delaney JR (1988) Infrared spectroscopic measurements of CO₂ and H₂O glasses in the Juan de Fuca Ridge basaltic glasses. *Earth Planet Sci Lett* 90:87–104
- Dohmen R, Becker HW, Chakraborty S (2007) Fe-Mg diffusion in olivine I: experimental determination between 700 and 1,200 degrees C as a function of composition, crystal orientation and oxygen fugacity. *Phys Chem Miner* 34(6):389–407
- Dohmen R, Chakraborty S (2007) Fe-Mg diffusion in olivine II: point defect chemistry, change of diffusion mechanisms and a model for calculation of diffusion coefficients in natural olivine. *Phys Chem Miner* 34(6):409–430
- EMSC—European-Mediterranean Seismological Centre (2010) EMSC website: <http://www.emsc-csem.org>. Accessed 01 Dec 2010
- Ferguson DJ, Barnie TD, Pyle DM, Oppenheimer C, Yirgu G, Lewi E, Kidane T, Carn S, Hamling I (2010) Recent rift-related volcanism in Afar, Ethiopia. *Earth Planet Sci Lett* 292(3–4):409–418
- Fine G, Stolper E (1986) Dissolved carbon dioxide in basaltic glasses: concentrations and speciation. *Earth Planet Sci Lett* 76:263–278
- Gerlach TM (1980) Investigation of volcanic gas analyses and magma outgassing from Erta 'Ale lava lake, Afar, Ethiopia. *J Volcanol Geotherm Res* 7(3–4):415–441
- Giordano D, Russell JK, Dingwell D (2008) Viscosity of magmatic liquids: a model. *Earth Planet Sci Lett* 271:123–134
- Harris AJL, Carniel R, Jones J (2005) Identification of variable convective regimes at Erta Ale Lava Lake. *J Volcanol Geotherm Res* 142(3–4):207–223
- Hauri E (2002) SIMS analysis of volatiles in silicate glasses, 2: isotopes and abundances in Hawaiian melt inclusions. *Chem Geol* 183(1–4):115–141
- Hirn B, Di Bartola C, Ferrucci F (2009) Combined use of SEVIRI and MODIS for detecting, measuring, and monitoring active lava flows at erupting volcanoes. *IEEE Trans Geosci Remote Sens* 47(2):2923–2930
- Irvine TN, Baragar WRA (1971) A guide to the chemical classification of the common volcanic rocks. *Can J Earth Sci* 8:523–548
- Ito M, Ganguly J (2006) Diffusion kinetics of Cr in olivine and ⁵³Mn-⁵³Cr thermochronology of early solar system objects. *Geochim Cosmochim Acta* 70(3):799–809
- Le Guern F, Carbonnelle J, Tazieff H (1979) Erta 'Ale lava lake: heat and gas transfer to the atmosphere. *J Volcanol Geotherm Res* 6(1–2):27–48
- Lesne P, Kohn S, Blundy J, Witham F, Botcharnikov R, Behrens H (2011) Experimental simulation of closed-system degassing in the system basalt-H₂O-CO₂-S-Cl. *J Petrol* 52:1737–1762
- Llewellyn EW, Manga M (2005) Bubble suspension rheology and implications for conduit flow. *J Volcanol Geotherm Res* 143(1–3):205–217
- Lowenstern JB, Mahood GA (1991) New data on magmatic H₂O contents of pantellerites with implications for petrogenesis and eruptive dynamics at Pantelleria. *Bull Volcanol* 54(1):78–83
- Mahatsente R, Jentzsch G, Jahr T (1999) Crustal structure of the Main Ethiopian Rift from gravity data: 3-dimensional modeling. *Tectonophysics* 313(4):363–382
- Milman-Barris MS, Beckett JR, Baker MB, Hofmann AE, Morgan Z, Crowley MR, Vielzeuf D, Stolper E (2008) Zoning of phosphorus in igneous olivine. *Contrib Mineral Petrol* 155(6):739–765
- Müller J (2010) MSG Level 1.5 Image data format description. Eumetsat documentation online EUM/MSG/ICD/105. http://www.eumetsat.int/groups/ops/documents/document/pdf_ten_05105_msg_img_data.pdfV6. Accessed 23 Feb 2010
- Nesbitt LM (1935) Hell-hole of creation: the exploration of Abyssinian Danakil. Alfred. A. Knopf, New York, p 382
- Newman S, Lowenstern JB (2002) VolatileCalc: a silicate melt-H₂O-CO₂ solution model written in Visual Basic for Excel. *Comput Geosci* 28(5):597–604
- Nichols ARL, Carroll MR, Hoskuldsson A (2002) Is the Iceland hot spot also wet? Evidence from the water contents of undegassed submarine and subglacial pillow basalts. *Earth Planet Sci Lett* 202(1):77–87
- Nichols ARL, Wysoczanski RJ (2007) Using micro-FTIR spectroscopy to measure volatile contents in small and unexposed inclusions hosted in olivine crystals. *Chem Geol* 242:371–384
- Oppenheimer C, Francis P (1997) Remote sensing of heat, lava and fumarole emissions from Erta Ale volcano, Ethiopia. *Int J Remote Sens* 18(8):1661–1692
- Pal R (2003) Rheological behaviour of bubble-bearing magmas. *Earth Planet Sci Lett* 207:165–179
- Pagli C, Wright TJ, Ebinger CJ, Yun S, Cann JR, Barnie T, Ayele A (2012) Shallow axial magma chamber at the slow-spreading Erta Ale Ridge. *Nat Geosci* 5284–5288. doi:10.1038/ngeo1414
- Pineau F, Javoy M (1994) Strong degassing at ridge crests: the behaviour of dissolved carbon and water in basalt glasses at 14°N, Mid-Atlantic Ridge. *Earth Planet Sci Lett* 123(1–3):179–198
- Prodehl C, Fuchs K, Mechie J (1997) Seismic-refraction studies of the Afro-Arabian rift system—a brief review. *Tectonophysics* 278(1–4):1–13
- Putirka K, Johnson M, Kinzler R, Longhi J, Walker D (1996) Thermobarometry of mafic igneous rocks based on clinopyroxene-liquid equilibria, 0–30 kbar. *Contrib Mineral Petrol* 123(1):92–108
- Putirka KD (2008) Thermometers and barometers for volcanic systems. *Minerals, inclusions and volcanic processes*. *Rev Min Geochem* 69:61–120

- Rollinson H (1993) Using geochemical data: evaluation, presentation, interpretation. Longman Scientific, New York
- Sawyer GM, Oppenheimer C, Tsanev VI, Yirgu G (2008) Magmatic degassing at Erta 'Ale volcano, Ethiopia. *J Volcanol Geotherm Res* 178(4):837–846
- Shishkina TA, Botcharnikov RE, Holtz F, Almeev RR, Portnyagin MV (2010) Solubility of H₂O and CO₂ bearing fluids in tholeiitic basalts at pressures up to 500 MPa. *Chem Geol* 277(1–2):115–125
- Spandler C, O'Neill H (2010) Diffusion and partition coefficients of minor and trace elements in San Carlos olivine at 1,300°C with some geochemical implications. *Contrib Mineral Petrol* 159(6):791–818
- Sun S, McDonough WF (1989) Chemical and isotopic systematics of oceanic basalts: implications for mantle composition and processes. In: Saunders AD, Norry MJ (eds) *Magmatism in the ocean basins*. *Geol Soc Sp* 42:313–345
- Tazieff H (1973) Erta Ale volcano. *Rev Geol Dyn Geogr* 15(4):437–441
- Varet J (1972) 03/1972 (CSLP 16–72) Card 1363 (06 March 1972). *Bulletin of the Global Volcanism Network*. Smithsonian Institute, Global Volcanism Program. www.si.edu. Accessed January 2011
- Varet J (1972) 05/1972 (CSLP 16–72) Card 1390 (10 May 1972). *Bulletin of the Global Volcanism Network*. Smithsonian Institute, Global Volcanism Program. www.si.edu. Accessed January 2011
- Vetsch P, Assefa G, Asfaw L (1992) 09/1992 (BGVN 17:09) *Bulletin of the Global Volcanism Network*. Smithsonian Institute, Global Volcanism Program. www.si.edu. Accessed January 2011
- Vetsch P, Caillet M, Haefeli S, Burgi P-Y (2003) 04/2003 (BGVN 28:04) *Bulletin of the Global Volcanism Network*. Smithsonian Institute, Global Volcanism Program. www.si.edu. Accessed January 2011
- Wilson SA (1997) The collection, preparation and testing of USGS reference material BCR-2, Columbia river, basalt. USGS Open-File Report 98-xxx
- Wolfenden E, Ebinger C, Yirgu G, Renne PR, Kelley SP (2005) Evolution of a volcanic rifted margin: Southern Red Sea, Ethiopia. *Geol Soc Am Bull* 117(7–8):846–864
- Wright R, Pilger E (2008) Satellite observations reveal little inter-annual variability in the radiant flux from the Mount Erebus lava lake. *J Volcanol Geotherm Res* 177(3):687–694
- Wright TJ, Ebinger CJ, Biggs J, Ayele A, Yirgu G, Keir D, Stork A (2006) Magma maintained rift segmentation at continental rupture in the 2005 Afar dyking episode. *Nature* 442:291–294
- Yirgu G, Philpotts A (2005) 09/2005 (BGVN 30:09) *Bulletin of the Global Volcanism Network*. Smithsonian Institute, Global Volcanism Program. www.si.edu. Accessed January 2011